UNIVERSITÄT ZU LÜBECK
INSTITUTE OF MATHEMATICS AND
IMAGE COMPUTING

Master's Thesis

Spatially Variant Deconvolution for Low Dose X-Ray Imaging

Johannes Lotz

Advisors

Prof. Dr. Jan Modersitzki
Institute of Mathematics and Image Computing
University of Lübeck

Prof. Dr. James G. Nagy
Department of Mathematics and Computer Science
Emory University

November 2011

MIC

IM FOCUS DAS LEBEN

EMORY
UNIVERSITY

MASTER'S THESIS

Spatially Variant Deconvolution in Low Dose X-Ray Imaging

A Mathematical Model to Improve Image Resolution in X-Ray Imaging with Thick Scintillators

submitted by	Johannes Lotz
Advisors	Prof. Dr. Jan Modersitzki
	Prof. Dr. James G. Nagy

November 2011

Institute of Mathematics and Image Computing
University of Lübeck
and
Department of Mathematics and Computer Science
Emory University

I had the great opportunity to do the research for this work at the Department of Mathematics and Computer Science of Emory University in Atlanta, Georgia.

I want to thank

James Nagy, Ioannis Sechopoulos,
Jan Modersitzki and Bernd Fischer

for their help and support in writing this thesis and for making my stay in Atlanta possible.

Abstract

X-ray imaging detectors are indispensable in modern medical diagnostics but since their radiation is potentially harmful, the radiation dose a patient is exposed to has to be kept as low as possible. One of the two predominant types of x-ray detectors are indirect detectors. They contain a scintillator crystal which converts incident x-ray radiation into light that is detected similarly to a digital photograph. One way to reduce the radiation dose required to produce an image in such a detector is to increase the thickness of the scintillator. However, scattering processes inside the scintillators cause the resulting image to be blurred.

The core of this thesis is to model the image recovery in these detectors as a spatially variant image reconstruction problem where a high number of discretized point spread functions (PSFs) is used to describe the image's blur. We present a method to compute these PSFs based on a few samples created by Monte Carlo simulations presented in [Badano and Sempau, 2006] and evaluate the image reconstruction on artificial data.

Contents

1 Introduction **1**

2 Digital X-Ray Imaging and Its Simulation **3**
2.1 Classical X-Ray Generation and Detection 3
2.1.1 Scattering and Absorption 5
2.1.2 Crystal Scintillators 5
2.2 Simulation of Light and X-Ray Scattering 8

3 Mathematical Methods for Image Restoration **11**
3.1 Image Acquisition as a Fredholm Integral Equation 11
3.1.1 Discrete Convolution 13
3.1.2 Regularization of the Reconstruction Problem 16
3.1.3 Conjugate Gradients Related Methods 20
3.2 Modeling Spatial Variance in the X-Ray Image Acquisition 24
3.3 Smooth Transitions Between Spatially Variant Point Spread Functions . . 25
3.3.1 Compensation of Boundary Artifacts 27
3.4 Fourier Transform for Fast Matrix Multiplication 28
3.4.1 Fast Fourier Transform 30
3.4.2 Modified Overlap-Add to Reduce the Problem Size 33
3.4.3 Preconditioning of the Iteration Matrix 34

4 Application of the Forward Model to Artificial X-Ray Imaging Data **37**

5 Evaluation of Calculated PSFs and Restored Images **43**
5.1 Interpolation of Spatially Variant Point Spread Functions 43
5.2 Reconstruction of Simulated X-Ray Images 43
5.2.1 Analysis of the Relative Error 46
5.2.2 Improvements in Image Contrast 50

6 Conclusion and Outlook **55**

Summary of Used Symbols and Abbreviations

The following symbols and abbreviations will be used throughout this work. In our notation, bold lowercase letters are reserved for vectors. Matrices and two dimensional arrays are printed in bold capital letters and scalars in regular letters.

d_1	thickness of the amorphous scintillator layer
d_2	thickness of the structured scintillator layer
x	true x-ray density, continuous
p	point spread function, continuous
b	blurred image, continuous
n	noise, continuous
$\mathbf{s}, s, \mathbf{t}$	spatial coordinates
$\mathbf{X}$	true x-ray density, 2D array of $L \times M$ pixels
N	$= LM$
$\mathbf{P}$	point spread function, 2D array
$\mathbf{B}$	blurred image, 2D array
$\mathbf{N}$	noise, 2D array
$\mathbf{x}$	true x-ray density, discrete vector form, $\mathbf{x} \in \mathbb{R}^N$
$\mathbf{p}$	point spread function, discrete vector form
$\mathbf{b}$	blurred image, discrete vector form
$\mathbf{n}$	noise, discrete vector form
$\mathbf{A}$	convolution matrix associated with $\mathbf{p}$
$\mathbf{U} = [\mathbf{u}_1, ..., \mathbf{u}_N]$	
$\mathbf{V} = [\mathbf{v}_1, ..., \mathbf{v}_N]$	unitary matrices of singular value decomposition (SVD)
$\mathbf{\Sigma}$	diagonal matrix of SVD with singular values
σ_i	singular values of $\mathbf{A}$
$\mathbf{\Sigma}_k^-$	"inverse" diagonal matrix of truncated SVD, $(\mathbf{\Sigma}_{i,i})_{i>k} = 0$

$\mathbf{A}_k^-$	"inverted" truncated SVD of $\mathbf{A}$
$\mathbf{x}^R$	regularized solution
$\mathbf{r}_i$	Residual $\mathbf{A}\mathbf{x}_i - \mathbf{b}$ in the i-th step of the CG or gradient descent method
$\mathbf{q}_i$	search direction of the CG or gradient descent method
$\mathbf{M}_i$	masking matrices corresponding to convolution matrices $\mathbf{A}_i$
$\mathbf{W}$	weight matrix to suppress border artifacts
$\mathbf{F}$	Fourier basis matrix
$\mathbf{\Lambda}_i$	diagonal matrix resulting from Fourier transform of $\mathbf{A}_i$
$\mathbf{C}$	preconditioning matrix approximating $\mathbf{A}$

QE	quantum efficiency
PSF	point spread function

1 Introduction

Beginning right after the discovery of x-ray radiation in the late 19th century, radiography has become more and more important in medicine during the last centuries [Assmus, 1995; Bernier et al., 2004]. In recent years, digital x-ray imaging has gained popularity because it reduces the radiation dose for the patient in many cases [Strotzer et al., 1998] and also makes it possible to offer computer-assisted diagnosis [Miller, 1999].

In medical applications, there are two classes of x-ray imaging devices that are distinguished by the way the incident x-ray energy is converted into an image. Direct x-ray detectors convert incident x-ray photons into electrical charges that are directed to capacitors associated to image pixels. Indirect detectors on the other hand, contain a scintillating crystal in which incident x-ray photons are converted into light that can then be detected similarly to photographs in common digital cameras. Which of these two detector classes should be used, depends on the application [Samei and Flynn, 2003].

While x-ray examinations are essential in modern medicine on the one hand, the exposure to this kind of radiation has to be minimized on the other hand because it is known to also cause cancer due to its ionizing properties [de González and Darby, 2004]. In current x-ray detectors, noise in the image is increased if the radiation dose is lowered. To overcome this trade-off, the performance of the detector has to be increased. One of the performance metrics of x-ray detectors is the quantum efficiency (QE), which is the ratio of absorbed to incident x-rays. In order to reduce the radiation dose the imaged patient is exposed to, it is desirable to achieve a high quantum efficiency.

One of the principal parameters that influence the QE positively is the thickness of the scintillator. In an ideal detector, all x-rays would be detected at the precise position at which they enter the scintillator. However, since all detectors have a QE of less than unity, not all incident x-rays are detected by the system. In addition, due to lateral spread of light photons and scattering inside the crystal, some x-ray energy is detected at incorrect locations resulting in an increased blur in images acquired with thicker scintillators [Nagarkar et al., 1998].

Approaches to limit the blur in the acquired image include improving the structure or

the material of the scintillator crystal. For example, in [Nagarkar et al., 1998] the authors presented a method to build columnar structured scintillator crystals that limit lateral spread and thus limit the blur in the acquired image. However, these approaches cannot completely prevent the blur.

Recent progress in simulation of the scattering processes in the scintillator have been made [Badano, 1999; Badano and Kanicki, 2001; Badano and Sempau, 2006] with the help of Monte Carlo techniques. Their results allow a mathematical modeling of the blur introduced in the image.

In this work we present a novel method to reduce the blur introduced in the acquired image. We model the image degradation caused by the scintillator as a spatially variant image restoration problem and introduce an interpolation framework to generalize the computational expensive physical simulations of the scattering process. At the time of this writing we are not aware of published computational approaches to reduce the blur in the image acquired by thick scintillators.

It was a great pleasure to do the research for this work in Spring and Summer of 2011 at Emory University together with Jim Nagy and Ioannis Sechopoulos. At designated points in this work, material is taken from an article that still is in preparation.

This work is organized as follows. In Chapter 2 the fundamentals x-ray imaging are discussed. Furthermore, the physical background of x-ray imaging and the simulation of the image degradation by scattering are outlined.

Chapter 3 deals with the mathematical forward model that describes the blurring process. The chapter starts with an introduction into the simplified spatial invariant and the extended spatial variant model for image blur. This is the basis for an interpolation model developed in this work, that is described in Section 3.2 and 3.3. In the following Section 3.4 we describe methods to accelerate the necessary computations.

Chapter 4 describes the details to apply the forward model to artificial x-ray imaging data. The performance of the image restoration with the calculated PSFs from our model is evaluated in Chapter 5. Finally, in Chapter 6 we draw the conclusions of this work and give an outlook to future research.

2 Digital X-Ray Imaging and Its Simulation

In this chapter we discuss the fundamentals of the image restoration problem in digital radiography. After describing the composition of an x-ray detection device, Section 2.1 follows the x-ray photons through the x-ray device from the source to the detector and summarizes the interactions taking place on this way. The method used to simulate these processes, especially the simulation of the interactions in the x-ray detector, is summarized in Section 2.2.

2.1 Classical X-Ray Generation and Detection

This heavily simplified overview of the physics in x-ray imaging is mainly taken from the books [Webb and Kagadis, 2003] and [Morneburg, 2010].

Radiography is a very popular tool in medical imaging, astronomy and crystallography [Nagarkar et al., 1998]. A planar digital x-ray imaging device as it is used in many medical applications, consists of a radiation source that emits x-ray photons and a photodetector that generates an image from incident x-ray photons. In the case of indirect detectors, a scintillator first converts x-ray photons into light that is then detected by a photodetector. A simplified layout of the image acquisition process is shown in Figure 2.1. If an object is placed between source and detector, a part of the x-ray photons is absorbed. The attenuation of the incident x-ray energy varies for different types of material and is stronger for bones and weaker for soft tissue, such that a contrast can be observed in the projection image generated in the detector.

X-Ray source The design of the x-ray source is common in most x-ray devices. It consists of an evacuated vessel that contains a negatively charged cathode and a positively charged anode. A potential difference is applied in between the two components. The cathode, consisting of a spirally coiled wire, is heated up to a temperature above 2000 ℃

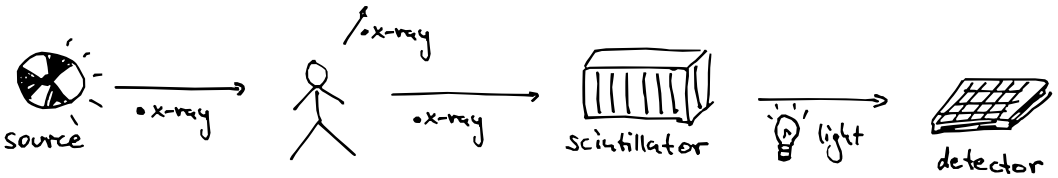

Figure 2.1: Sketch of the x-ray imaging process. X-ray photons are emitted from the detector and partly attenuated in the patient. The scintillator transforms the incident x-ray photons into light that can be detected by a photodetector similar to those used in digital photo cameras.

by an electric current flowing through it. At this temperature, few electrons move away from their nuclei and are dragged towards the anode due to the potential difference.

On its way to the anode, the electrons are further accelerated such that they obtain a high kinetic energy. Eventually, the electrons hit the anode and a small portion of their kinetic energy is converted into x-rays. This is due to two processes, referred to as *bremsstrahlung radiation* and *characteristic radiation.* The former occurs in interaction of the accelerated electron with nuclei, the later in interaction with electrons in the anode.

Bremsstrahlung radiation *Bremsstrahlung radiation* is generated if an electron approaches a nucleus and is deflected from its path by the nucleus' positive charge. The electron loses parts of its energy which is reemitted in form of an x-ray. Since the electron does not lose all its energy at once, it can emit several x-rays of different energies while penetrating the outer layer of the anode. The x-ray with the highest possible energy is generated if all of the electron's kinetic energy is transformed into one x-ray at once.

Characteristic Radiation If an accelerated electron collides with an electron located in one of the inner shells of an anode atom, the inner electron can be ejected from the atom. In this case, the hole in the electron shell resulting from the missing electron is filled by an electron from a higher shell that loses potential energy in form of an x-ray, this is called *characteristic radiation.* In contrast to bremsstrahlung radiation that emits a continuous spectrum of x-ray energies, characteristic radiation only generates x-rays of specific discrete energies corresponding to the difference of potential energy between two electron shells. Therefore, the energy pattern of this kind of radiation is characteristic for the anode's material.

The x-rays generated in the anode are generated in all directions, but all x-rays except for those emitted in the direction of the x-ray tube output window are absorbed by the x-ray tube's shielding. The output window is positioned so that the x-rays that travel through it are emitted towards a detector. If an object is inserted into the path between emitter and

detector, the x-ray photon can either be scattered, absorbed or not interact with the object at all. The contrast in the image that is generated in the detector is due to the difference in the amount of x-ray photons that are absorbed or scattered by the different tissues in the body and hence do not reach the detector.

2.1.1 Scattering and Absorption

The two ways of scattering of the x-ray photon that occur in x-ray imaging are coherent (or Rayleigh) scattering and incoherent or *Compton scattering*. Coherent scattering is a non-ionizing interaction with the object's electrons. The kinetic energy of an x-ray photon is completely absorbed and converted into an oscillation of an electron that reradiates the same amount of energy in form of an x-ray. The new x-ray photon is emitted into a random direction. Compton scattering occurs if an x-ray photon hits an electron that absorbs a portion of the photons energy and is ejected. During the collision, the x-ray photon's path and its energy is altered.

If the x-ray photon hits a tightly bound electron in the object, a large amount or all of its kinetic energy is absorbed and its remaining energy is likely to be lost in subsequent collisions before leaving the object. In this case, the x-ray photon is absorbed. A small amount of characteristic x-ray radiation is generated in this process, but is also absorbed in the object due to its low energy.

Those x-ray photons that are neither absorbed nor scattered leave the object without any interaction and hit the detector. The two most important classes of detectors are those with direct conversion on the one hand, where x-ray photons are converted directly into electric charges and those with indirect conversion on the other hand [Chotas et al., 1999]. We focus on the second class, in which striking x-ray photons are first converted into visible light which can be detected by a thin-film-transistor (TFT) or a charge-coupled device (CCD) [Chotas et al., 1999]. Results from [Samei and Flynn, 2003] show that radiography devices with indirect conversion have a high efficiency, especially in clinical settings where the detected image has low contrast and is degraded by noise.

2.1.2 Crystal Scintillators

The materials used in indirect detectors can emit a small quantity of light when they are hit by some kind of radiation. This property is called *luminescence* and can be observed in some organic crystals and liquids, but also in other inorganic materials such as gases,

plastics and glasses [Leo, 1994]. In many modern x-ray detectors a doped crystal of cesium iodide (CsI) is used. In this work, we consider a thallium-doped cesium iodide scintillator. A tiny flash of light is emitted if an x-ray photon hits an electron in the scintillator and transfers enough energy to push it to a higher energy level. During the subsequent inverse transition back to a lower energy level the electron reemits parts of its energy in form of visible light that can be detected using a photomultiplier. If the reemission occurs instantly, this property is also referred to as fluorescence and more details can be found in [Leo, 1994, p. 157].

Scintillators, especially in the crystalline form that we consider, allow the use of light sensors very similar to the ones used in today's digital photo cameras to measure incident x-rays and their energy.

A disadvantage of crystal scintillators is the limiting trade-off between spatial resolution and radiation stopping power [Nagarkar et al., 1998]. An x-ray photon entering the scintillator can be scattered from its path by the same x-ray-matter interactions described above. In addition, the emitted light photon is also subject to scattering once it has been generated inside the scintillator. For this reason, a thick crystal results in a loss of spatial resolution but in a gain in QE. The loss of spatial resolution can be described as a blur in the resulting image. To overcome this limitation, Nagarkar et al. [Nagarkar et al., 1998] proposed a columnar crystal that limits the scattering processes to a narrow region. A simplified scheme of the x-ray detector is shown in in Figure 2.2.

An important observation for the model that will be developed later in this work is that the characteristics of the scattering depends on the angle in which the x-ray photons hit the scintillator. The left photon beam in Figure 2.2 scatters in average symmetrically around its center which does not hold for the right photon beam. Figure 2.3 illustrates the difference in the images resulting from the two x-ray photon beams together with corresponding profile plots.

Although the columnar structure reduces the scattering in the crystal, it cannot completely do away with the blur in the image and a significant amount of scattering is still present. This can also be observed in the images in Figure 2.3 that would only show a very narrow spot if no scattering would occur in the scintillator. The blur occurring in the acquired images limits the thickness of the crystal and therefore also limits the x-ray stopping power in today's x-ray detectors. Table 2.1 shows the increase of QE in thicker scintillators for two different x-ray energies, measured in kVp describing the peak energy of the x-ray spectrum. Scintillation based x-ray detectors as they are currently used for example in digital mammography work with scintillator thicknesses of up to 0.2 mm [Smith, 2003; Baldelli et al., 2010]. At this thickness, less than 60 % of the x-ray photon energy that is incident on a the scintillator interacts with it. The remaining 40 % leave the

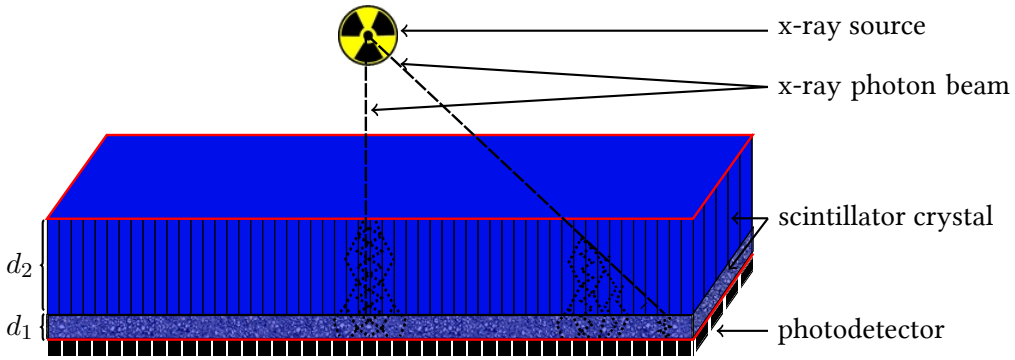

Figure 2.2: Schematic model of the x-ray-detector and the scattering of light photons. The scintillator consists of a structured layer of thickness d_2 and an amorphous layer of thickness d_1. Two exemplary x-ray photon beams are shown with the resulting schematic scattering (dotted lines) of the generated light photons.

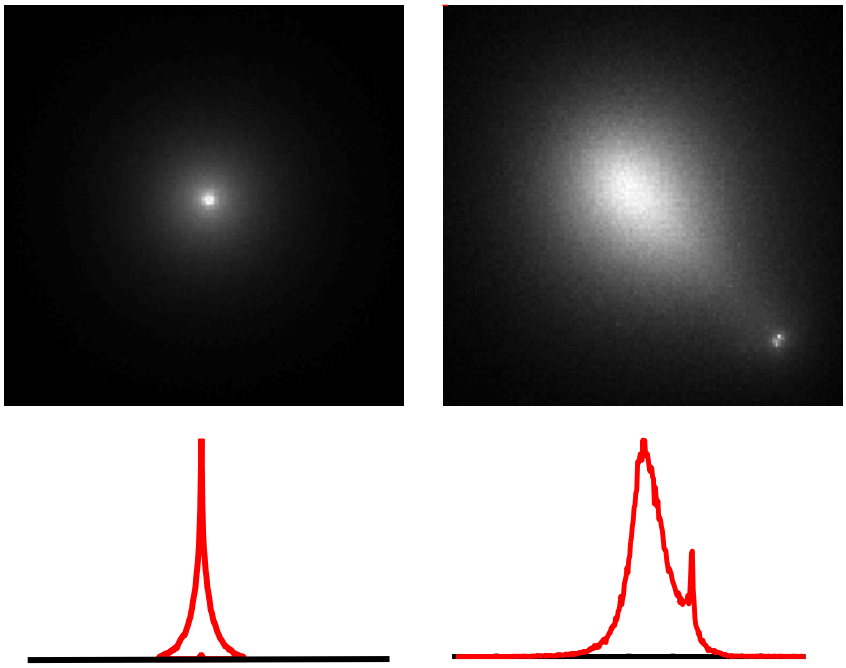

Figure 2.3: Simulated images and their profile plots resulting from two photon beams hitting a scintillator of thickness 1.5 mm in different angles. The profile plots in the second row show the main diagonal of the image. Left: Photon beam hitting the center of the scintillator perpendicularly. Right: Photon beam hitting the scintillator at a wider angle.

Table 2.1: Estimated quantum efficiency for varying scintillator thickness from 0.2 to 2 mm for the two x-ray energy spectra considered in this work.

CsI Thickness (mm)	QE at 80kVp	QE at 120kVp
0.200	56.4%	37.9%
0.600	88.5%	69.6%
0.800	93.6%	77.3%
1.200	97.8%	86.5%
1.600	99.2%	91.5%
2.000	99.7%	94.4%

scintillator undetected. Depending on the energy spectrum used this percentage can also be worse. At an energy spectrum of 120kVp, less than 40% of the x-ray photons that the patient has been exposed to can be detected. Fortunately, this number can be increased to more than 90% if thicker scintillators could be used in clinical settings. In order to lower the radiation dose for a patient, thick scintillator crystals with high stopping power could be used if we were able to avoid the blur in the image.

2.2 Simulation of Light and X-Ray Scattering

As a first step, we simulate the processes in the scintillator crystal with a tool called *MANTIS* proposed by Badano and Sempau in [Badano and Sempau, 2006]. Their model combines the Monte Carlo approaches of two software packages called Penelope [Salvat, Fernández-Varea, Acosta, and Sempau, 2003] and Detect-II [Badano and Kanicki, 2001; Badano, 1999]. Penelope is used to model the interactions of electrons and x-rays with matter. This includes the effects of x-rays and electrons on matter described in the previous chapter as well as other interactions out of scope of this work. Detect-II models the optical transport inside the crystal but also at the boundaries between the columns and towards the photodetector.

The processes inside the scintillator cannot be modeled analytically but only on a statistical basis. This means that for, say, a collision of two particles, e.g. an x-ray photon and an electron, the outcome depends on parameters that are not explicitly known but that follow a certain probability distribution. To obtain a reliable approximation of the result of a series of such collisions, the series has to be simulated repeatedly while changing the probabilistic parameters randomly, according to its probability distribution. This is

done in a Monte Carlo experiment. Using random numbers, a Monte Carlo experiment samples outcomes for each of the processes involved in the particle transport in the scintillator according to their probabilities. If a sufficiently high number of these samples is computed, the combined outcomes constitute a good estimate for the location and energy of the light photons leaving the scintillator. As this work deals mostly with the images resulting from such simulations, the reader is referred to the original paper [Badano and Sempau, 2006] or to [Binder and Heermann, 2010] for a discussion of these models.

3 Mathematical Methods for Image Restoration

In this chapter, we extend the previously described simulations to model the blurring introduced in the scintillator as an image restoration problem. The first section explains the basic model to describe the image restoration problem and introduces different regularization methods to deal with noisy images. In the previous chapter we have shown that the scattering inside the scintillator depends on the position at which it is hit by incident x-ray photons. In Section 3.2 we extend the image restoration model to take this dependency into account. To compute this extended model, a higher number of PSFs than available from the Monte Carlo simulations with MANTIS are needed. Section 3.3 presents a new method to calculate these PSFs based on few simulated samples. In Section 3.4 methods to accelerate the computation by taking advantage of the structure of the mathematical model are discussed.

3.1 Image Acquisition as a Fredholm Integral Equation

We define the function $x : \mathbb{R}^2 \to \mathbb{R}$ as a model for the underlying but but inaccessible true x-ray intensity that occurs just before the x-rays reach the scintillator. This is the image that would occur at the upper red frame in Figure 2.2. Furthermore, we define $p : \mathbb{R}^2 \times \mathbb{R}^2 \to \mathbb{R}$ as the point spread function (PSF) that is used to define the blurring operation. In some cases it can be given analytically by a specific function, but in most cases it has to be determined experimentally or by simulations. The PSF is the response of a system to a point source, an input image that consists of only one very bright and narrow point. This kind of input, for example, can be achieved by an extremely narrow photon beam, as the ones mentioned in Section 2.1.2. The result of the blurring process is contaminated by some kind of additive noise that is defined as $n : \mathbb{R}^2 \to \mathbb{R}$. The resulting light photon density is defined as the function $b : \mathbb{R}^2 \to \mathbb{R}$. This is the signal that is acquired at the location of the lower red frame in Figure 2.2 by a photodetector. Given this data, the aim of this work is to reconstruct the true image modeled by x. Following [Nagy et al., 1998] we model the blurring process by the Fredholm integral equation of

thefirst kind

$$\int_{\Omega} p(\mathbf{s}, \mathbf{t}) x(\mathbf{t})\, d\mathbf{t} + n(\mathbf{s}) = b(\mathbf{s}). \tag{3.1}$$

Here, $\mathbf{s} \in \mathbb{R}^2$ are spatial coordinates and Ω is the region containing the area of the detector, thus the region of support of b.

Fredholm integral equations of the first kind are common in image processing and many other fields, see for example [Hansen, 1992]. They consist of a kernel p and an unknown function x in the integral whose boundaries do not depend on $\mathbf{s}$. The right hand side b is often a result of a measurement.

One of the challenges in solving the integral in Equation (3.1) is the spatial variance, that is discussed in detail in Section 3.2. The main point is that the PSF p depends not only on the position in the image but also on the position of the center of the corresponding point source.

However, to better discuss the discretization and regularization in the following pages, spatial variance can be neglected. We first consider the simplified spatially invariant case, where the same point spread function is applied to all locations of the ground truth image, such that

$$p(\mathbf{s}, \mathbf{t}) = p(\mathbf{s} - \mathbf{t}).$$

Since we are dealing with digitally recorded images and discrete pixel values, we discretize the integral equation. The photodetector basically consists of very small cells that correspond to the pixels in the image it produces such that the cell $\mathcal{C}_{l,m}$ corresponds to the (l, m)-th pixel. We denote the edge length of each cell with δ and illustrate the discretization in Figure 3.1. In each of these cells, the incident light photons are summed up during the image detection. Because the location closest to all counted incident photons of each cell is its center, we use a cell centered grid where each cell in the grid corresponds to a cell in the detector.

We denote a vertical, vector-like representation of this array with a small letter $\mathbf{b}$ and a two dimensional representation with capital letter $\mathbf{B}$. Each cell $\mathcal{C}_{l,m}$ of this array collects the energy of all incident photons inside its boundary. Therefore, the l, m-th entry of the discretized signal array $\mathbf{B}(l, m)$ corresponds to the integral

$$\mathbf{B}(l, m) = \mathbf{b}(l + mL) = \int_{\mathcal{C}_{l,m}} b(\mathbf{s})\, d\mathbf{s},\ l = 1, ..., L,\ m = 1, ..., M$$

over the domain of the cell $\mathcal{C}_{l,m}$ of the continuous signal $b(\mathbf{s})$.

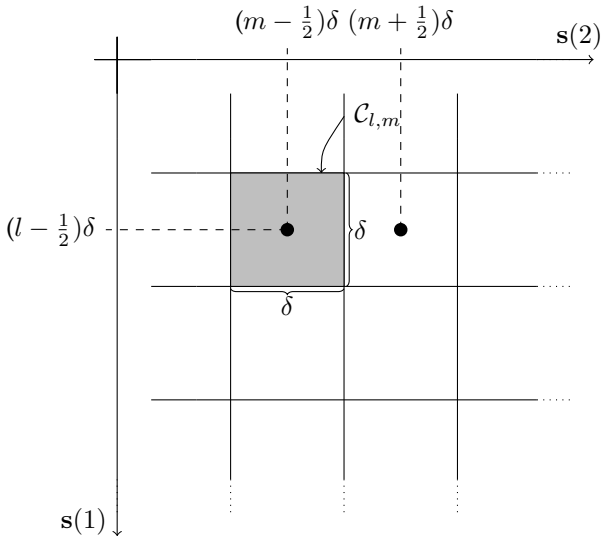

Figure 3.1: Cell centered grid corresponding to the cells in the photodetector. Each cell $\mathcal{C}_{l,m}$ (in gray) of dimension $\delta \times \delta$ is centered around the coordinates $\big((l-\frac{1}{2})\delta, (m-\frac{1}{2})\delta\big)$

.

We define the two-dimensional arrays

$\mathbf{X} \in \mathbb{R}^{L\times M}$ as the discretized x-ray density, the *model for the true image*,

$\mathbf{P} \in \mathbb{R}^{L\times M}$ as the discretized PSF,

$\mathbf{B} \in \mathbb{R}^{L\times M}$ as the discretized photon density, the *blurred image* and

$\mathbf{N} \in \mathbb{R}^{L\times M}$ as noise.

Note that we use matrix notation to better describe the data stored in these arrays but that these arrays do not necessarily have any operator properties. With $N = LM$ the vertical arrays can be represented as vectors $\mathbf{x}, \mathbf{p}, \mathbf{b}, \mathbf{n} \in \mathbb{R}^N$ analog to the two dimensional arrays above.

3.1.1 Discrete Convolution

The discretized blurring operation can be written as a discrete convolution. To introduce the convolution we consider the one dimensional case with discrete functions $x_c, p_c : \mathbb{Z} \to \mathbb{R}$ that represent the arrays $\mathbf{x}$ and $\mathbf{p}$ but have additional information about the

entries with indices $l < 1$ or $l > N$ that are outside the boundaries of the arrays. The discrete function $b_c : \mathbb{Z} \to \mathbb{R}$ representing $\mathbf{b}$ is the result of the discrete convolution

$$b_c = p_c * x_c \text{ with}$$
$$b_c(l) = \sum_{k=-\inf}^{\inf} p_c(l-k)\, x_c(k) \tag{3.2}$$

[Mertins, 1996]. We apply the convolution on the data stored in arrays $\mathbf{x}$ and $\mathbf{p}$. Assumptions for data outside the boundaries are called boundary conditions and their choice depends on the data that they are applied to.

Two possible choices are zero boundary conditions and circular boundary conditions. Zero boundary conditions means that all values outside the boundary are assumed to be zero whereas with circular boundary conditions the array is "wrapped around" such that its last entry is followed directly by its first entry.

Figure 3.2 shows an illustration of the discrete convolution with zero boundary conditions. The array $\mathbf{p}$ is flipped and shifted above $\mathbf{x}$, beginning with one overlapping entry. To compute the first entry of $\mathbf{b}$, the values of the overlapping entries are multiplied. Subsequently, the shift is increased by one. Each pair of overlapping entries is multiplied and all the products are summed up to obtain the next value of $\mathbf{b}$.

Each value of $\mathbf{b}$ is a linear combination of the elements of $\mathbf{x}$ weighted by entries of $\mathbf{p}$. Therefore, the convolution can also be written as a matrix multiplication of $\mathbf{x}$ with a matrix $\mathbf{A} \in \mathbb{R}^{N \times N}$, where each row of $\mathbf{A}$ contains a differently shifted copy of $\mathbf{p}$. If zero boundary conditions are assumed, the non-overlapping entries of $\mathbf{p}$ are ignored and the remaining entries of $\mathbf{A}$ are filled with zeros. In the case of circular boundary conditions, the array $\mathbf{p}$ is wrapped around in each row such that all the entries of $\mathbf{A}$ are filled. The matrix in the two dimensional case, its structure and the resulting consequences are discussed in Section 3.4.

Using the convolution, the discrete blurring process defined by a PSF $\mathbf{P}$ of the image $\mathbf{X}$, represented in $\mathbf{A}$ and $\mathbf{x}$ can be written as

$$\mathbf{b} = \mathbf{A}\mathbf{x} + \mathbf{n}.$$

A certain amount of x-ray radiation will pass the object in most cases such that the detected image $\mathbf{b}$ will have much greater values than the magnitude of the possibly negative noise $\mathbf{n}$. Therefore, it is possible to neglect non-negativity constraints on $\mathbf{b}$ or $\mathbf{x}$.

For later reference, we summarize the simplified model of the image blurring process as

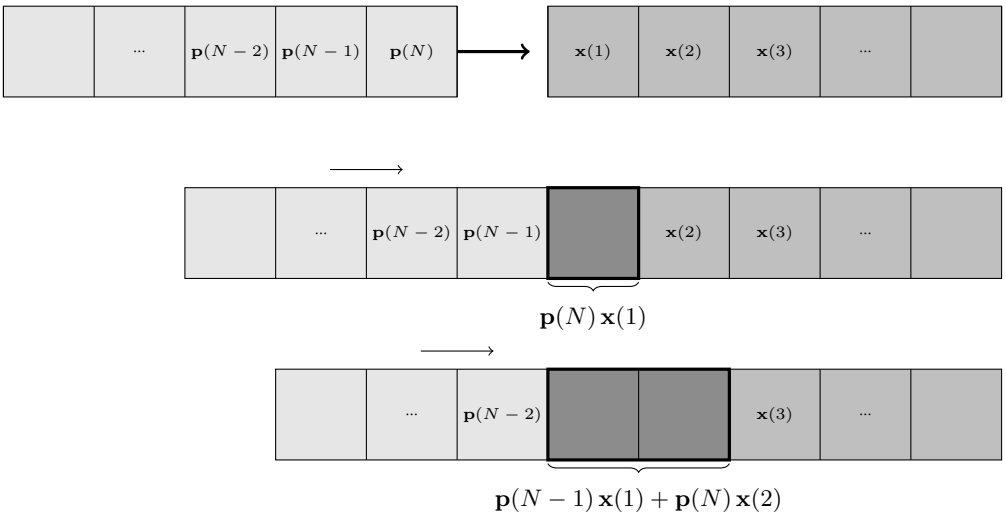

Figure 3.2: One dimensional discrete convolution of arrays $\mathbf{p}$ and $\mathbf{x}$ with zero boundary conditions resulting in an array $\mathbf{b}$. The array $\mathbf{p}$ is flipped and shifted subsequently over $\mathbf{x}$ such that the overlap increases. The values of two overlapping entries are multiplied and added up to obtain a value of $\mathbf{b}$ at each step.

follows.

Spatially invariant blur. *The acquisition of an image* $\mathbf{b} \in \mathbb{R}^N$ *that is degraded by spatially invariant blur defined by a matrix* $\mathbf{A} \in \mathbb{R}^{N \times N}$ *is modeled by the linear system*

$$\mathbf{b} = \mathbf{A}\mathbf{x} + \mathbf{n}, \tag{3.3}$$

with unknown noise $\mathbf{n}$.

There are numerous approaches to solve image restoration problems similar to Equation (3.3). These include SVD and Conjugate Gradient type methods [Hansen, 1998] that are discussed in this chapter but also e.g. SOR based methods [Strakhov and Vorontsov, 2008]. Problems arising from integral equations like (3.1) are ill-posed since the blurring kernel represented by the PSF has smoothing properties that naturally eliminate edges and other high frequency components [Hansen, 1998]. The inverse operation of deblurring the image will thus increase the high frequency components present in the blurred

image. Unfortunately, also high frequency perturbations such as noise and round-off errors as they are inevitable in data acquisition and discretization would be amplified by a naive inverse operation [Hansen, Nagy, and O'Leary, 2006].

3.1.2 Regularization of the Reconstruction Problem

In order to discuss the problems arising in the reconstruction of images affected by noise, we first give a numerical example that illustrates the need for regularization and then describe the *singular value decomposition* that can be used to analyze the spectral properties of the image restoration problem.

To stress the importance of regularization, we consider the exemplary system

$$\mathbf{A}\mathbf{x} = \mathbf{b} \text{ where} \tag{3.4}$$
$$\mathbf{A} = \begin{bmatrix} 1 & & \\ & \sigma_2 & \\ & & \sigma_3 \end{bmatrix} \text{ and } \mathbf{b} = \begin{bmatrix} 1 \\ 0 \\ b_3 \end{bmatrix}.$$

The eigenvalues of $\mathbf{A}$ are set to small arbitrary values of $\sigma_2 = 0.1$ and $\sigma_3 = 0.001$. The solution $\mathbf{x} = [1\ 0\ b_3/\sigma_3]^{\mathrm{T}}$ of the unperturbed system can be computed easily. We now add a perturbation that can also be seen as noise and obtain

$$\begin{aligned} \begin{bmatrix} 1 & & \\ & \sigma_2 & \\ & & \sigma_3 \end{bmatrix} \tilde{\mathbf{x}} &= \begin{bmatrix} 1 \\ 0 \\ b_3 \end{bmatrix} + \begin{bmatrix} 0.01 \\ 0.01 \\ 0.01 \end{bmatrix} \\ \Rightarrow \tilde{\mathbf{x}} &= \begin{bmatrix} 1 & & \\ & \frac{1}{\sigma_2} & \\ & & \frac{1}{\sigma_3} \end{bmatrix} \left(\begin{bmatrix} 1 \\ 0 \\ b_3 \end{bmatrix} + \begin{bmatrix} 0.01 \\ 0.01 \\ 0.01 \end{bmatrix} \right) \\ &= \begin{bmatrix} 1 \\ 0 \\ b_3/\sigma_3 \end{bmatrix} + \begin{bmatrix} 0.01 \\ 0.01/0.1 \\ 0.01/0.001 \end{bmatrix} = \begin{bmatrix} 1 \\ 0 \\ b_3/\sigma_3 \end{bmatrix} + \begin{bmatrix} 0.01 \\ 0.1 \\ 10 \end{bmatrix}. \end{aligned} \tag{3.5}$$

The result of this computation shows that regularization is necessary as the relative error $\frac{\|\tilde{\mathbf{x}}-\mathbf{x}\|_2}{\|\mathbf{x}\|_2} \gg 1$ is large for small values of b_3.

Singular Value Decomposition

Before discussing the actual regularization we analyze the spectral properties of general matrices using a singular value decomposition as described in [Hansen et al., 2006].

A decomposition of a matrix $\mathbf{A}$ into factors

$$\mathbf{A} = \mathbf{U}^{\mathrm{T}}\mathbf{\Sigma}\mathbf{V}$$
$$\text{where } \mathbf{\Sigma} = \text{diag}(\sigma_1, ..., \sigma_N),\ \sigma_1 \geq \sigma_2 \geq ... \geq \sigma_N$$

and $\mathbf{U} = [\mathbf{u}_1, ..., \mathbf{u}_N]$ and $\mathbf{V} = [\mathbf{v}_1, ..., \mathbf{v}_N] \in \mathbb{R}^{N \times N}$ are orthogonal matrices is defined as a singular value decomposition (SVD). Such a decomposition can be used to write the inverse matrix $\mathbf{A}^{-1}$ as

$$\mathbf{A}^{-1} = \mathbf{V}^{\mathrm{T}}\mathbf{\Sigma^{-1}}\mathbf{U} \text{ with } \mathbf{\Sigma}^{-1} = \text{diag}(\frac{1}{\sigma_1}, ..., \frac{1}{\sigma_N}).$$

With this expression, the solution $\mathbf{x}$ of the system $\mathbf{Ax} = \mathbf{b}$ can be written as

$$\begin{aligned} \mathbf{x} &= \mathbf{A}^{-1}\mathbf{b} \\ &= \mathbf{V}^{\mathrm{T}}\mathbf{\Sigma^{-1}}\mathbf{U}\mathbf{b} \\ &= \sum_{i=1}^{N} \frac{\mathbf{u}_i^{\mathrm{T}}\mathbf{b}}{\sigma_i}\mathbf{v}_i \end{aligned} \tag{3.6}$$

As mentioned before, noise is an inevitable factor in digital image detection. In Equation (3.6) we see that the solution $\mathbf{x}$ is composed of vectors $\mathbf{v}_i$ that are weighted by factors $(\mathbf{u}_i^{\mathrm{T}}\mathbf{b})/\sigma_i$. The oscillations in $\mathbf{v}_i$ tend to increase with increasing i. They can lead to amplified noise in the resulting image which of course is unwanted.

Common approaches to regularize the solution of image restoration problems and to reduce the influence of noise and numerical errors to the solution include truncated singular value decomposition (TSVD) [Hansen, 1990] and also iterative approaches such as the CG method [Hestenes and Stiefel, 1952; Hanke et al., 1993]. Another well known method is Tikhonov regularization [Tikhonov and Arsenin, 1977] that we will not discuss in this work.

The idea common to the TSVD method discussed in the next section and also to the other regularization approaches discussed in Section 3.1.3 is to damp the influence of smaller singular values. The information in the regularized solution is preserved using the singular vectors $\mathbf{v}_k,\ k \ll N$, corresponding to larger singular values.

Truncated SVD

The truncated SVD (TSVD) uses the decomposition of $\mathbf{A}$ into singular vectors to compute a regularized solution. Therefore, the representation of the inverse of $\mathbf{A}$ in the SVD in

Equation (3.6) is modified to obtain a regularized, spectrally truncated "inverse" matrix

$$\mathbf{A}_k^- = \mathbf{V}^{\mathrm{T}}\mathbf{\Sigma}_k^-\mathbf{U},$$

where only the k largest singular values are considered by setting

$$\mathbf{\Sigma}_k^- = \mathrm{diag}(\frac{1}{\sigma_1}, ..., \frac{1}{\sigma_k}, 0, .., 0),\ k < N.$$

If we calculate an approximation of the true image using the truncated SVD with

$$\begin{aligned}\mathbf{x}^R &= \mathbf{A}_k^-\mathbf{b} \\ &= \mathbf{V}^{\mathrm{T}}\mathbf{\Sigma}_k^-\mathbf{U}\mathbf{b} \\ &= \sum_{i=1}^{k}\frac{\mathbf{u}_i^{\mathrm{T}}\mathbf{b}}{\sigma_i}\mathbf{v}_i\end{aligned}$$

the high frequency components $\mathbf{v}_i^*\mathbf{b}$ for $i > k$ corresponding to smaller singular values of $\mathbf{A}$ are not part of the solution.

With this first regularization technique at hand, we can again consider the example from the Equations (3.4) - (3.5) and compute a regularized solution with $k = 2$.

The regularized solution $\mathbf{x}^R$ then is

$$\begin{aligned}\mathbf{x}^R &= \begin{bmatrix}1 & & \\ & \frac{1}{\sigma_2} & \\ & & \mathbf{0}\end{bmatrix}\left(\begin{bmatrix}1\\0\\b_3\end{bmatrix} + \begin{bmatrix}0.01\\0.01\\0.01\end{bmatrix}\right) \\ &= \begin{bmatrix}1\\0\\\mathbf{0}\end{bmatrix} + \begin{bmatrix}0.01\\0.1\\\mathbf{0}\end{bmatrix}\end{aligned} \tag{3.7}$$

Comparing the regularized solution $\mathbf{x}^R$ with the exact solution $\mathbf{x} = [1\ \ 0\ \ b_3/\sigma_3]^{\mathrm{T}}$ by computing the relative error $e_r = \frac{\|\mathbf{x}^R - \mathbf{x}\|_2}{\|\mathbf{x}\|_2}$, we note that the error mainly depends on b_3/σ_3. Two cases can be distinguished.

- For $b_3 \approx 0$ we observe that $\mathbf{x} \approx \mathbf{x}^R$. ☺
- For $b_3 \gg 0$ the relative error approaches $e_r \to 1$ and the regularized solution is a worse approximation than in the first case. ☹

Discrete Picard Condition

Whether a regularized solution is a good approximation for the true solution can be determined as follows. In [Hansen, 1990] the *discrete Picard condition* is introduced and Hansen shows that if this condition is satisfied, then the regularized solution $\mathbf{x}^R$ of a noise perturbed system approximates the solution of the corresponding unperturbed system.

The discrete Picard condition *is satisfied if the coefficients* $\mathbf{u}_i^T\mathbf{b}$ *on the average decay faster than the singular values* σ_i *which means that the factors* $(\mathbf{u}_i^T\mathbf{b})/\sigma_i$ *decay for increasing* i*.*

Again, coming back to the example in Equation (3.7) we note that a singular value decomposition of $\mathbf{A}$ consists of the singular vectors $\mathbf{u}_1 = \mathbf{v}_1 = \mathbf{e}_1$, $\mathbf{u}_2 = \mathbf{v}_2 = \mathbf{e}_2$ and $\mathbf{u}_3 = \mathbf{v}_3 = \mathbf{e}_3$ such that

$$\mathbf{A} = \begin{bmatrix} 1 & & \\ & \sigma_2 & \\ & & \sigma_3 \end{bmatrix} = \begin{bmatrix} 1 & & \\ & 1 & \\ & & 1 \end{bmatrix} \begin{bmatrix} 1 & & \\ & \sigma_2 & \\ & & \sigma_3 \end{bmatrix} \begin{bmatrix} 1 & & \\ & 1 & \\ & & 1 \end{bmatrix} = \mathbf{U}^T\mathbf{\Sigma}\mathbf{V}. \tag{3.8}$$

With this decomposition in mind we can check if the two cases for b_3 discussed above satisfy the discrete Picard condition and conclude the numerical example by finding:

- For $b_3 \approx 0$ the discrete Picard condition is satisfied because $\sigma_2 > \sigma_3 = 0.001 > 0 = \mathbf{e}_2^{\mathrm{T}}\mathbf{b} = \mathbf{e}_3^{\mathrm{T}}\mathbf{b}$. In this case we observe that $\mathbf{x} \approx \mathbf{x}^R$. ☺
- For $b_3 \gg 0$ the discrete Picard condition is violated because $\sigma_2 > \sigma 3 = 0.001 \ll b_3 = \mathbf{e}_3^{\mathrm{T}}\mathbf{b}$. In this case, the exact solution has a large value in its third component that cannot be covered by the regularized solution. ☹

The discrete Picard condition introduces a trade-off between spectral properties in the image and magnitude of the blur introduced by the PSF. For example for PSFs of Gaussian shape, broader PSFs lead to increased blur and their singular values decay faster than those of narrower PSFs [Hansen et al., 2006]. This means that the reconstruction of images containing structures corresponding to higher frequencies is limited if the image is strongly blurred. In this section, we have seen that if the discrete Picard condition is satisfied, regularization can improve the solution dramatically.

3.1.3 Conjugate Gradients Related Methods

Another regularization method that leads essentially to similar results as TSVD, is to use an iterative solver such as the method of conjugate gradients (CG) or other Krylov subspace methods and to stop the iteration early [Hanke, 2001]. This is particularly useful if the system cannot be solved directly as it often occurs in large linear systems because memory consumption and processing time do not scale very well in direct solvers [Benzi, 2002]. In this work, we focus on the LSQR method presented in [Paige and Saunders, 1982] as it has proven to be one of the most efficient methods to solve large ill-posed problems [Hanke, 2001]. As we will discuss in the following section, this algorithm has regularizing properties that are very similar to those of the TSVD method without explicitly calculating the decomposition.

Before discussing its regularizing properties, we will first introduce the CG method from an optimization point of view starting with the method of gradient descent. This part is mostly taken from [Nocedal and Wright, 1999].

The *Conjugate Gradients* (CG) method [Hestenes and Stiefel, 1952] solves linear systems $\mathbf{Ax} = \mathbf{b}$ with symmetric and positive definite matrices $\mathbf{A} \in \mathbb{R}^{N \times N}$. It can be derived from the following method of gradient descent applied to the objective function

$$f = \frac{1}{2}\mathbf{x}^T\mathbf{Ax} - \mathbf{b}^T\mathbf{x} \rightarrow \text{ min} \tag{3.9}$$

which has the same unique solution as the linear system.

Listing 3.1: Gradient Descent

```
choose arbitrary x_0
for i=1:k
  r_i = A x_{i-1} - b        % calculate the gradient
  q_i = -r_i                 % choose search direction
  α = (r_i^T q_i)/(q_i^T A q_i)   % calculate step length
  x_i = x_{i-1} + α q_i      % iterate
end
```

Here, the search direction is the direction of the negative gradient which is also called the direction of steepest descent. At each iteration the one dimensional minimizer along $f(\alpha) = \mathbf{x}_i + \alpha\mathbf{q}_i$ of the objective function in Equation (3.9) is computed.

The CG methods is similar but the search direction $\mathbf{q}_i$ is chosen differently. Given a set $\{\mathbf{q}_1, \cdots, \mathbf{q}_N\}$ of N non-zero directions that are conjugated with respect to $\mathbf{A}$ such that

$\mathbf{q}_i^{\mathrm{T}}\mathbf{A}\mathbf{q}_j = 0,\ \forall i \neq j$, the solution of the linear system can be computed in N steps in exact arithmetic.

In this process which is based on the Lanczos method [Saad, 1996, p. 175], the iterates $\mathbf{x}_i$ are elements of an extending Krylov subspace

$$\mathbf{x}_i \in \mathbf{x}_0 + \text{span}\left\{\mathbf{r}_0, \mathbf{A}\mathbf{r}_0, ..., \mathbf{A}^{i-1}\mathbf{r}_0\right\}$$

and an orthogonal basis for this subspace is constructed.

The directions are computed as a linear combination of the residual $\mathbf{r}_i$ and the previous direction

$$\mathbf{q}_i = -\mathbf{r}_i + \beta_i \mathbf{q}_{i-1}. \tag{3.10}$$

Enforcing conjugacy, the coefficients β_i are defined by multiplying $\mathbf{q}_{i-1}^{\mathrm{T}}\mathbf{A}$ to (3.10) such that

$$\begin{aligned} \mathbf{q}_{i-1}^{\mathrm{T}}\mathbf{A}\mathbf{q}_i &= (\mathbf{q}_{i-1}^{\mathrm{T}}\mathbf{A})(-\mathbf{r}_i + \beta_i\mathbf{q}_{i-1}) \\ \Rightarrow \beta_i\mathbf{q}_{i-1}\mathbf{A}\mathbf{q}_{i-1} &= \mathbf{q}_{i-1}\mathbf{A}\mathbf{r}_i \\ \Rightarrow \beta_i &= \frac{\mathbf{q}_{i-1}\mathbf{A}r_i}{\mathbf{q}_{i-1}\mathbf{A}\mathbf{q}_{i-1}}. \end{aligned}$$

The CG method is very efficient because only the vector $\mathbf{q}_{i-1}$ is needed to compute $\mathbf{q}_i$ which is automatically conjugated to the previous directions as well.

By induction, it can be shown, that

- the directions $\mathbf{q}_i,\ i = 1, ..., N$ of the CG method are indeed conjugated with respect to $\mathbf{A}$,
- the residuals are orthogonal $\mathbf{r}_i^{\mathrm{T}}\mathbf{r}_j = 0$ for $i \neq j$ and
- $\mathbf{q}_i$ and $\mathbf{r}_i$ are contained in the *Krylov subspace* of degree i, defined as

$$\mathcal{K}_i(\mathbf{r}_0, \mathbf{A}) = \text{span}\{\mathbf{r}_0, \mathbf{A}\mathbf{r}_0, ..., \mathbf{A}^i\mathbf{r}_0\}.$$

A proof can be found in [Nocedal and Wright, 1999, p. 109].

LSQR Method

In many applications, the matrix $\mathbf{A}$ is not symmetric. If the CG method is applied to the system

$$\mathbf{A}^{\mathrm{T}}\mathbf{A}\mathbf{x} = \mathbf{A}^{\mathrm{T}}\mathbf{b} \tag{3.11}$$

the resulting method is known as CGNE. Due to the additional multiplication with the transpose, the condition number is squared compared to the original system and the convergence can slow down [Saad, 1996, p. 195]. An alternative that, in exact arithmetic, produces the same results is the *LSQR method* [Paige and Saunders, 1982]. It is also based on the Lanczos method but instead considers the system

$$\begin{bmatrix} \mathbf{I}_N & \mathbf{A} \\ \mathbf{A}^{\mathrm{T}} & 0 \end{bmatrix} \begin{bmatrix} \mathbf{r} \\ \mathbf{x} \end{bmatrix} = \begin{bmatrix} \mathbf{b} \\ \mathbf{0} \end{bmatrix}$$

which has the same solution as the normal equation in Equation (3.11) and does not increase the condition number.

Regularizing Properties of the LSQR Method

In the following paragraphs we describe the regularizing properties of the LSQR method as reported in [Chung and Nagy, 2010]. LSQR is based on the Lanczos bidiagonalization procedure [Golub and Kahan, 1965] and transforms the matrix $\mathbf{A} \in \mathbb{R}^{N\times N}$ iteratively into a bidiagonal matrix $\mathbf{G}_k \in \mathbb{R}^{k\times k}$. After k iterations that depend on the right hand side $\mathbf{b}$ the LSQR-algorithm results in the factorization into matrices $\mathbf{T}_k \in \mathbb{R}^{m\times k}$, $\mathbf{U}_k \in \mathbb{R}^{m\times k+1}$ with orthonormal columns and the bidiagonal matrix $\mathbf{G}_k$ such that

$$\mathbf{A}\mathbf{T}_k = \mathbf{U}_k\mathbf{G}_k. \tag{3.12}$$

The singular values of $\mathbf{G}_k$ approximate the singular values of $\mathbf{A}$ [Doicu et al., 2010] depending on their relative spread. In early iterations, those singular values with the highest relative spread are the ones that are best approximated [Golub et al., 1981].

For image restoration problems, the singular values of $\mathbf{A}$ decay to zero and build clusters near zero. To illustrate this, we show the spectrum of an exemplary PSF in Figure 3.3. The top plot shows a cluster of singular values close to zero while the bottom plot shows a relatively large spread between the larger singular values. As the relative spread for these small singular values is very low due to the clustering, larger singular values are approximated first.

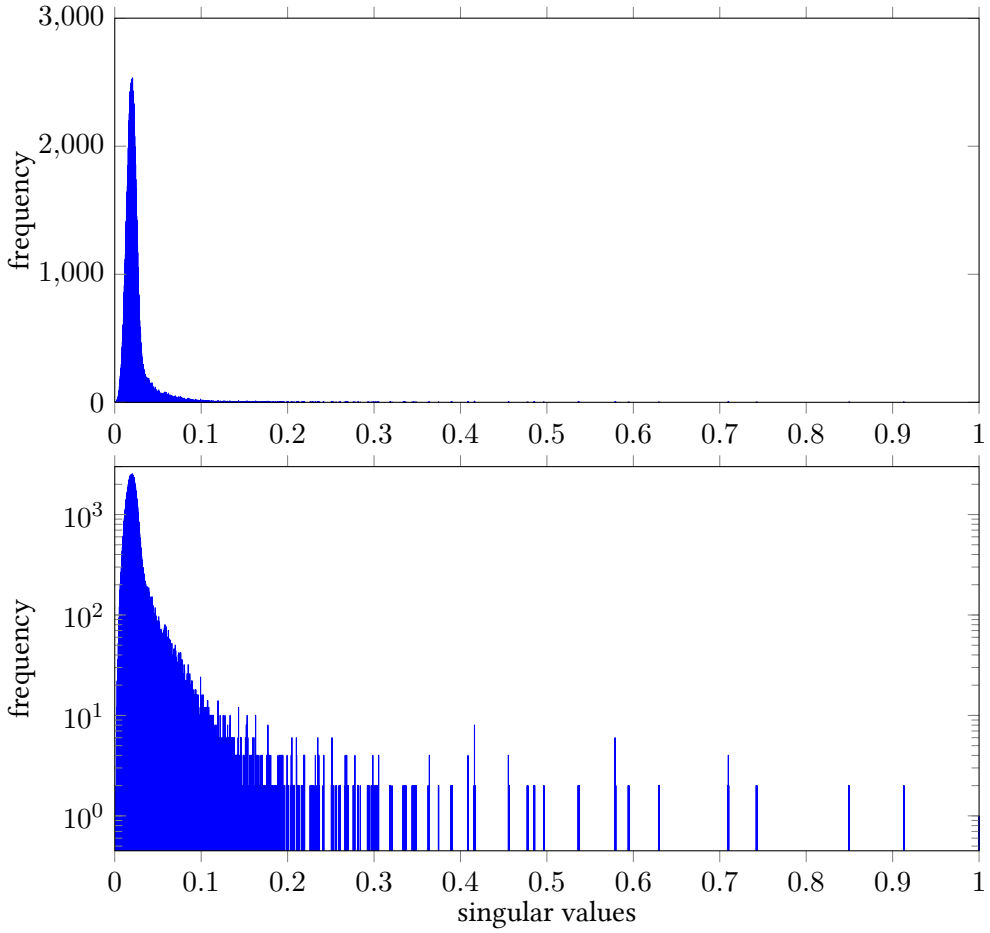

Figure 3.3: Linear (top) and semilogarithmic (bottom) histogram plot of the spectrum of an examplary PSF showing a large cluster of singular value close to zero and several smaller clusters. Singular values are scaled to $[0\ 1]$.

Hence, LSQR leads to a similar result as the truncated SVD with the difference that the filtering is more abrupt if the TSVD is used. The number of iteration steps k of the LSQR method can be used as a regularization parameter.

3.2 Modeling Spatial Variance in the X-Ray Image Acquisition

In Section 3.1 the blurring process has been modeled as a spatially invariant convolution. However, the construction of the scintillator detector described in Section 2.1.2 requires a more complex model that supports different blur on different positions on the detector. In this section we introduce a spatially variant model that extends the simplified spatial invariant model in Equation (3.3).

We consider again the Fredholm integral equation from Equation (3.1)

$$\int_{\Omega} p(\mathbf{s}, \mathbf{t}) x(\mathbf{t})\, d\mathbf{t} + n(\mathbf{s}) = b(\mathbf{s})$$

but discretize it without the simplification $p(\mathbf{s}, \mathbf{t}) = p(\mathbf{s} - \mathbf{t})$.

The unsimplified integral equation leads to the spatially variant model described in [Nagy et al., 1998], where the PSF depends on the position of the point source. Different parts of the acquired image have been affected by different point spread functions. These parts of the image are isolated by premultiplying a diagonal masking matrix $\mathbf{M}_i \in \mathbb{R}^{N \times N}$ with

$$(\mathbf{M}_i)_{j,j} = \begin{cases} 1 & \text{if pixel } j \text{ belongs to region } i \\ 0 & \text{otherwise.} \end{cases} \tag{3.13}$$

which leads to a piecewise constant approximation of the spatial variance. Inside a region, spatial invariance is assumed. Using masks, these regions can be as small as an individual pixel which allows a fine grained approximation. Furthermore this model can be extended to a linear or higher order approximation by lifting the restriction to binary values in $\mathbf{M}_i$. With this assumption we can extend the forward model to calculate the blurred image $\mathbf{b}$ from a known true image $\mathbf{x}$ and known matrices $\mathbf{A}_i$ and $\mathbf{M}_i$. With simulated noise $\mathbf{n}$ the blurring process can be modeled as

$$\mathbf{b} = \sum_{i=1}^{k} \mathbf{A}_i \mathbf{M}_i \mathbf{x} + \mathbf{n}, \tag{3.14}$$

where $\mathbf{A}_i$ encodes the PSF corresponding to the point source located at the center of the i-th region and k is the overall number of regions.

3.3 Smooth Transitions Between Spatially Variant Point Spread Functions

To compute the blurred image according to the spatially variant model, a high number of PSFs is needed. The process of generating PSFs with MANTIS using Monte Carlo simulations described in Section 2.2 is computationally very expensive because each photon has to be simulated individually. For this reason, it is impractical to compute all the PSFs with this method.

In this section we present an interpolation approach that computes PSFs for arbitrary locations on the detector based on a few a priori known samples. Two of these samples are shown in the left and right image in Figure 3.4. The aim is to calculate a smooth transition consisting of intermediate PSFs between two or more PSF samples.

A direct pixelwise interpolation was analyzed first. Here, each pixel of the interpolated image is calculated independently of its neighbors based on the pixels in the PSF samples. This approach produces moving artifacts that are shown in the center image in Figure 3.4. This behavior is opposed to smooth transitions in the sense expected from the physical model. Figure 3.4 also shows that the main obstacle for a successful pixelwise interpolation is the narrower of the two circular shapes. Our strategy is therefore to first remove this shape and use the direct interpolation on the remaining image.

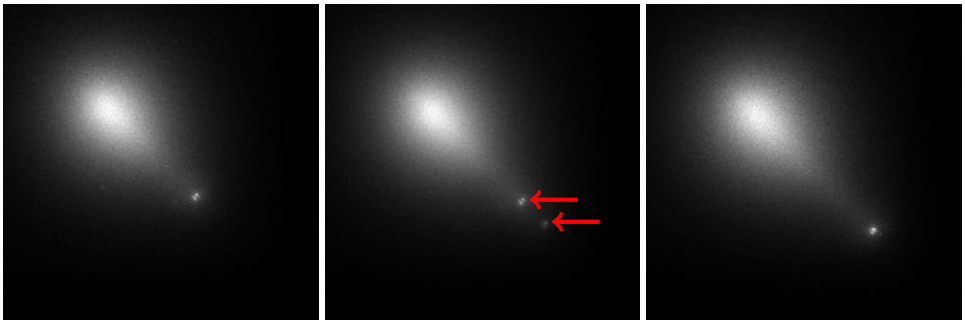

Figure 3.4: Moving artifacts occurring in direct pixel-wise interpolation. Left and right images are PSF samples simulated with MANTIS. The center image is the result of a direct pixelwise interpolation.

The following scheme first calculates PSFs for point sources on a straight line from the detector center to its lower right corner. Afterwards, PSFs corresponding to point sources on any straight line subtending the detector center can be obtained by rotating the PSFs by the same angle the line is rotated. Therefore only few samples corresponding to point

source positions on a straight line are needed to calculate all remaining PSFs. In the following paragraphs we assume this line to connect the upper left with the lower right corner of the image.

Let $\mathbf{P} \in \mathbb{R}^{m \times n}$ be the array containing the discretized PSF and assume that this array is square such that $m = n$. We extract a vector $\bar{\mathbf{p}} = \text{diag}(\mathbf{P})$ containing the diagonal elements from the image corresponding to the line connecting all point source positions. From the diagonal $\bar{\mathbf{p}}$ we calculate a set $\mathcal{S}_{\bar{\mathbf{p}}}$ containing the locations of certain local maxima (or peaks) by comparing neighboring pixel values and enforcing a minimal distance d_{min} between two candidate peaks such that

$$\begin{aligned}\mathcal{S}_{\bar{\mathbf{p}}} := \{i \in \{1, ..., N\} \,|\, \bar{\mathbf{p}}(i) > \bar{\mathbf{p}}(i+1) > ... > \bar{\mathbf{p}}(i+d_{min}),\\ \bar{\mathbf{p}}(i) > \bar{\mathbf{p}}(i-1) > ... > \bar{\mathbf{p}}(i-d_{min})\}.\end{aligned}$$

Examination of various PSF has shown that the centers of the two circular shapes usually correspond to the two highest peaks. Their coordinates $s_1, s_2 \in \{1, ..., N\}$ are obtained from $\mathcal{S}_{\bar{\mathbf{p}}}$ by

$$\begin{aligned}s_1 &= \min \{i \in \mathcal{S}_{\bar{\mathbf{p}}} \,|\, \bar{\mathbf{p}}(i) \geq \bar{\mathbf{p}}(j) \,\forall i \neq j \in \mathcal{S}_{\bar{\mathbf{p}}}\}\\ s_2 &= \min \{i \in \mathcal{S}_{\bar{\mathbf{p}}} \setminus \{s_1\} \,|\, \bar{\mathbf{p}}(i) \geq \bar{\mathbf{p}}(j) \,\forall i \neq j \in \mathcal{S}_{\bar{\mathbf{p}}} \setminus \{s_1\}\},\end{aligned}$$

where taking the minimal index assures that only one value is returned if more than one local maximum has the same height.

The height of the local maxima is not sufficient to decide which one is narrower. For cases where the two peaks are very close together, even the location has shown to be unreliable. We select the narrower Gaussian by comparing the right differential quotients

$$s^* = \underset{s_1, s_2}{\text{argmax}} \left(\bar{\mathbf{p}}(s_i) - \bar{\mathbf{p}}(s_i + \epsilon)\right), \, \epsilon \in \mathbb{N}.$$

and choosing the steeper one. As s^* is defined on the main diagonal of the PSF array. this leads to the position $\mathbf{s}^* = (s^*, s^*)$ of the narrow Gaussian shape in the two dimensional point spread function image $\mathbf{P}$. After the location of the narrow peak is determined, it is removed from the image. To this aim, a region of radius ρ around $\mathbf{s}^*$ is chosen. The pixel values in this region are set by cubic interpolation based on the region $\{\mathbf{x} \in \mathbb{R}^2, \rho^2 < \|\mathbf{x} - \mathbf{s}^*\|_2^2 \leq (2\rho)^2\}$ surrounding the peak. The resulting images without the narrow Gaussian can now be interpolated pixelwise because the moving artifacts do no longer occur. However, the resulting images are incomplete because the narrow Gaussian is missing.

To restore the narrow Gaussians in the pixel-wise interpolated images, their positions are interpolated based on their positions in the sample images. A model Gaussian with fixed width is added to the images at this position.

At this point, arbitrary PSFs corresponding to point sources on a straight line can be computed. The remaining PSF whose point sources are not located at this line can be obtained by rotation. Figure 3.5 shows an illustration of the interpolation scheme.

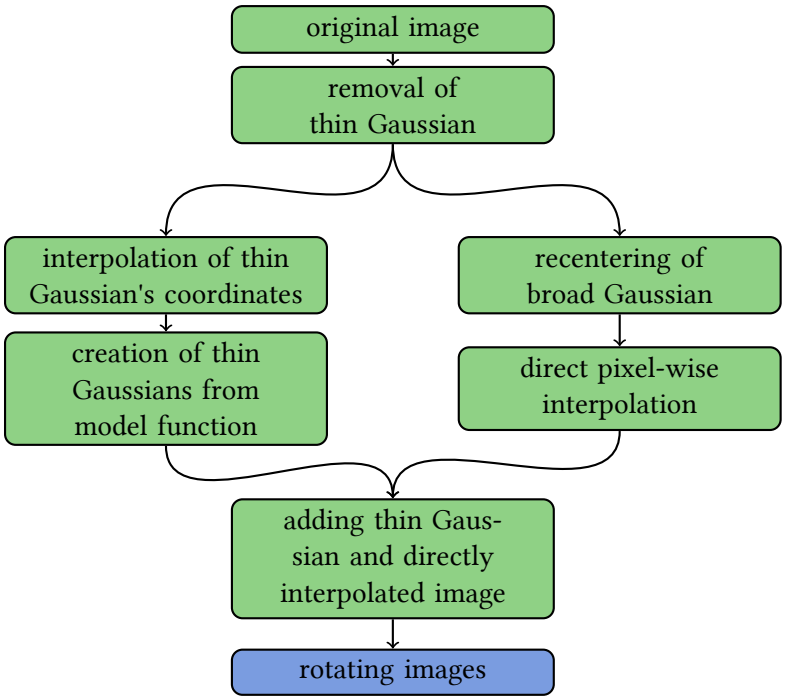

Figure 3.5: Interpolation scheme for PSF images.

3.3.1 Compensation of Boundary Artifacts

A disadvantage of the piecewise constant discretization of spatial variance is the resulting difference between adjacent PSFs occuring at the interface between regions. However, these artifacts can be compensated as shown below.

Being independent of the image, the artifacts can be minimized with the help of a diagonal weight matrix $\mathbf{W} \in \mathbb{R}^{N \times N}$ that is premultiplied to Equation (3.14) resulting in the

updated forward model

$$\mathbf{b} = \mathbf{W}^{-1} \sum_{i=1}^{k} \mathbf{A}_i \mathbf{M}_i \mathbf{x} + \mathbf{n}.$$

The diagonal of $\mathbf{W} = \text{diag}(\mathbf{w})$ can be computed by initializing $\mathbf{W}$ as the identity and applying the blur matrix to an hypothetical true image $\mathbf{1} \in \mathbb{R}^N$ consisting of only ones such that

$$\mathbf{w} = \mathbf{A}\mathbf{1}.$$

In this section we have presented a model to describe the image acquisition processes in terms of a discrete linear system, that can be summarized as follows.

Discretized spatially variant blur. *The acquisition of an image $\mathbf{b} \in \mathbb{R}^N$ that is degraded by spatially variant blur defined by matrices $\mathbf{W}^{-1}\mathbf{A}_i \in \mathbb{R}^{N \times N}$ and regions of the image selected by masking matrices $\mathbf{M}_i$ is modeled by the linear system*

$$\mathbf{b} = \mathbf{A}\mathbf{x} + \mathbf{n} = \mathbf{W}^{-1} \sum_{i=1}^{k} \mathbf{A}_i \mathbf{M}_i \mathbf{x} + \mathbf{n}, \tag{3.15}$$

from the hypothetical true image $\mathbf{x}$ with unknown noise $\mathbf{n}$.

3.4 Fourier Transform for Fast Matrix Multiplication

In Section 3.2 the image acquisition process has been modeled as a linear system represented by a blurring matrix $\mathbf{A} = \sum_{i=1}^{k} \mathbf{A}_i \mathbf{M}_i$. Regularizing methods like the LSQR algorithm that use this model to reconstruct an approximation of the underlying true image have been described in Section 3.1.3. In Equation (3.15), the matrix multiplication $\mathbf{A}_i \mathbf{M}_i \mathbf{x}$ has to be evaluated k times, where k is the total number of regions used to approximate spatial variance. As the error in the approximation is lower for smaller regions, this number can be high. For typical images of at least 200×200 pixels, matrices of size 40000×40000 have to be computed if the calculations are executed in the matrix form shown in Equation (3.15). The following section describes methods to accelerate these calculations.

The matrices $\mathbf{A}_i$ are usually dense. Building these matrices in memory and computing the matrix-vector product is therefore computationally expensive but can be performed efficiently in $\mathcal{O}(N \log(N))$ operations using discrete Fourier transforms [Brigham and Morrow, 1967]. The multiplication of the image vector $\mathbf{x}$ with the blurring matrix $\mathbf{A}_i$ is identical to the two-dimensional convolution of the image $\mathbf{X}$ with the PSF $\mathbf{P}_i \in \mathbb{R}^{L \times M}$ as described in Section 3.1 [Hansen et al., 2006].

Assuming circular boundary conditions, $\mathbf{A}_i \in \mathbb{R}^{LM \times LM}$ from Equation (3.15) is a block circulant matrix with circulant blocks $\mathbf{T}_k \in \mathbb{R}^{M \times M}$ of the form

$$\mathbf{A}_i = \begin{bmatrix} \mathbf{T}_{\frac{L}{2}} & \mathbf{T}_{\frac{L}{2}-1} & \dots & \mathbf{T}_1 & \mathbf{T}_L & \dots & \mathbf{T}_{\frac{L}{2}+1} \\ \mathbf{T}_{\frac{L}{2}+1} & \mathbf{T}_{\frac{L}{2}} & \ddots & & & & \\ \vdots & \ddots & \ddots & & & & \\ \mathbf{T}_1 & & & \ddots & & & \\ \mathbf{T}_L & & & & \ddots & & \\ \vdots & & & & & \ddots & \\ \mathbf{T}_{\frac{L}{2}-1} & & & & & & \mathbf{T}_{\frac{L}{2}} \end{bmatrix}$$

where

$$\mathbf{T}_k = \begin{bmatrix} \mathbf{p}_{\frac{M}{2},k} & \mathbf{p}_{\frac{M}{2}-1,k} & \dots & \mathbf{p}_{1,k} & \mathbf{p}_{M,k} & \dots & \mathbf{p}_{\frac{M}{2}+1,k} \\ \mathbf{p}_{\frac{M}{2}+1,k} & \mathbf{p}_{\frac{M}{2},k} & \ddots & & & & \\ \vdots & \ddots & \ddots & & & & \\ \mathbf{p}_{M,k} & & & \ddots & & & \\ \mathbf{p}_{1,k} & & & & \ddots & & \\ \vdots & & & & & \ddots & \\ \mathbf{p}_{\frac{M}{2}-1,k} & & & & & & \mathbf{p}_{\frac{M}{2},k} \end{bmatrix}$$

and $\mathbf{p}_{k,l} = \mathbf{P}_{i_{(k,l)}}$ is the (k,l)-th element of the PSF in matrix form. Due to this particular structure, there exists a diagonalization of the matrix A such that

$$\begin{aligned} \mathbf{A}_i = \mathbf{F}^* \mathbf{\Lambda}_i \mathbf{F} \Leftrightarrow \mathbf{F}\mathbf{A}_i &= \mathbf{\Lambda}_i \mathbf{F} \\ \Rightarrow \mathbf{F}\mathbf{A}_i(:,1) &= \mathbf{\Lambda}_i \mathbf{F}(:,1) = \mathbf{\Lambda}_i \mathbf{1}, \end{aligned}$$

where the entries of the diagonal matrix $\mathbf{\Lambda}_i \in \mathbb{C}^{N \times N}$ are identical to the discrete two-dimensional Fourier transform of the first column of $\mathbf{A}_i$ [Davis, 1994]. $\mathbf{F}$ is the discrete two-dimensional discrete Fourier transform matrix. Taking the block circulant structure

into account, the first column of $\mathbf{A}_i$ is identical to the circular shifted and vectorized array $\mathbf{P}_i$ that represents the PSF [Hansen et al., 2006].

Other than circular boundary conditions can be used by embedding the image in a larger image where the pixels out side the original image domain are determined according to the desired boundary condition. For instance, zero boundary conditions can be implemented by embedding the images in a larger image consisting of zeros [Nagy et al., 2004]. This can be combined with an overlap-add approach as described in [Oppenheim and Schafer, 1975] where small patches of the image are treated separately. This will be presented in Section 3.4.2. With the resulting larger, zero padded images, all calculations can be done assuming circular boundary conditions. This approach is used for a first evaluation of the methods presented in this work and will be extended in future work.

Finally, the complete blurring matrix is assembled in the equation

$$\mathbf{b} = \mathbf{A}\mathbf{x} = \mathbf{W}^{-1}\,\mathbf{F}^{*}\sum_{i=1}^{k}\mathbf{\Lambda}_i\,\mathbf{F}\,\mathbf{M}_i\,\mathbf{x}. \tag{3.16}$$

In each iteration of the LSQR method described in Section 3.1.3, a multiplication with the transpose of $\mathbf{A}$ has to be computed. In this transpose matrix multiplication

$$\mathbf{A}^{T}\mathbf{x} = \sum_{i=1}^{k}\mathbf{M}_i\,\mathbf{F}^{*}\,\mathbf{\Lambda}_i^{*}\,\mathbf{F}\,\mathbf{W}^{-1}\,\mathbf{x}.$$

the diagonal masking matrix $\mathbf{M}_i$ is premultiplied to each summand. For this reason the non-zero region of the result is known before the computation which makes it easier to compute the convolution.

3.4.1 Fast Fourier Transform

The computation of Equation (3.16) requires one forward and one backward Fourier transform for each masked region. As we will see, the direct computation of the discrete Fourier transform is inefficient and a number of algorithms for faster and more efficient computation have been developed. These algorithms are commonly summarized as *Fast Fourier Transforms* (FFT). As they are important tools used in many applications [Bracewell, 1978], we give an overview of their principles in the next section. The description is mostly based on the books [Proakis and Manolakis, 1996] and [Mertins, 1996].

To perform the Fourier transform, the FFTW implementation is used [Frigo and Johnson, 2005]. FFTW libraries are included in MATLAB and are also available for a variety of programming languages. The library consists of different FFT algorithms and uses a planner to select the most appropriate algorithm for each data set. Most of the commonly used FFT algorithms are based on a divide-and-conquer approach where the problem is decomposed into smaller problems. We assume a signal $\mathbf{x} = (\mathbf{x}(j))_{j=1:N}$ of length $N = LM$, where $L, M \in \mathbb{N}$. The direct one-dimensional *discrete Fourier Transform* (DFT) can be written as a matrix multiplication of the Fourier basis matrix $\mathbf{F} \in \mathbb{C}^{N\times N}$ with the discrete signal $\mathbf{x} \in \mathbb{C}^N$:

$$\begin{aligned}\mathbf{F}\mathbf{x} &= \left(\sum_{j=0}^{N-1} \mathbf{x}(j) e^{-i2\pi jk/N}\right)_{k=0,1,\ldots,N-1} = \left(\sum_{j=0}^{N-1} \mathbf{x}(j) W_N^{kj}\right)_{k=0,1,\ldots,N-1} \\ &= \begin{bmatrix} 1 & 1 & \cdots & 1 \\ 1 & W_N & \cdots & W_N^{N-1} \\ \vdots & \vdots & & \vdots \\ 1 & W_N^{N-1} & \cdots & W_N^{(N-1)^2} \end{bmatrix} \mathbf{x}, \text{ where } W_N = e^{-i2\pi/N}.\end{aligned} \tag{3.17}$$

The computation of Equation (3.17) needs N^2 complex multiplications and $N(N-1)$ additions such that the computational complexity is $\mathcal{O}(N^2)$.

Reordering the vector $\mathbf{x}(j)$ into an array $\mathbf{X}(l, m)$ with

$$\begin{aligned} j &= l + mL \\ l, p &= 0, ..., L-1 \\ m, q &= 0, ..., M-1 \end{aligned}$$

the above statement can be rewritten as

$$\hat{\mathbf{X}}(p, q) = \sum_{l=0}^{L-1} \sum_{m=0}^{M-1} \mathbf{X}(l, m)\, W_N^{(Mp+q)(mL+l)} \tag{3.18}$$

to compute an array containing the Fourier transform of $\mathbf{x}$ in the same array structure. We observe that

$$W_N^{(Mp+q)(mL+l)} = W_N^{MpmL}\, W_N^{Mpl}\, W_N^{qmL}\, W_N^{ql}$$

and simplify the factors

$$\begin{aligned} W_N^{MpmL} &= W_N^{Npm} = e^{-i2\pi} = 1, \\ W_N^{Mpl} &= W_{N/M}^{pl} = W_L^{pl}, \\ W_N^{qmL} &= W_{N/L}^{qm} = W_M^{qm} \end{aligned}$$

such that Equation (3.18) can be written as

$$\begin{aligned}\hat{\mathbf{X}}(p,q) &= \sum_{l=0}^{L-1}\sum_{m=0}^{M-1}\mathbf{X}(l,m)\,W_L^{pl}\,W_M^{qm}\,W_N^{ql} \\ &= \sum_{l=0}^{L-1} W_L^{pl} \underbrace{\left[\sum_{m=0}^{M-1}\mathbf{X}(l,m)\,W_M^{qm}\right]}_{=\mathbf{Y}(l,q),\text{computed } LM \text{ times}} W_N^{ql} \\ &= \sum_{l=0}^{L-1} W_L^{pl} \underbrace{\mathbf{Y}(l,q)\,W_N^{ql}}_{LM \text{ multiplications}} .\end{aligned}$$

The decomposed transform needs $\mathcal{O}(LM^2)$ operations (multiplications and additions) for the inner brace with the M-point DFT, $LM = N$ multiplications and $\mathcal{O}(L^2M)$ operations for the L-point DFT in the last line. Together, the computational complexity of the decomposed DFT is

$$\begin{aligned}&\mathcal{O}(LM^2) + \mathcal{O}(N) + \mathcal{O}(L^2M) \\ =&\mathcal{O}(N(M+L+1)) = \mathcal{O}(N(M+L)).\end{aligned}$$

Assuming that the signal length is a power of 2, $N = 2^k$, $k \in \mathbb{N}$, which can be achieved easily by zero padding, the decomposition can be repeated $log_2(N)$ times with $M = 2$. Therefore, using the FFT algorithm, the computational complexity of the DFT can be reduced to

$$\mathcal{O}(N(M+L)) = \mathcal{O}(N(2 + \underbrace{2 + \ldots + 2}_{\log_2(N)-2 \text{ times}})) = \mathcal{O}(N \log_2(N))$$

compared to $\mathcal{O}(N^2)$ in Equation (3.18).

The two dimensional DFT of an image can be obtained by first transforming each column by a one dimensional DFT and then transforming the rows of the result again in a second step. Hence, the two-dimensional DFT matrix $\mathbf{F}_{LM} \in \mathbb{C}^{N\times N}$ can be constructed with a Kronecker product from two one-dimensional DFT matrices $\mathbf{F}_L \in \mathbb{C}^{L\times L}$ and $\mathbf{F}_M \in \mathbb{C}^{M\times M}$ [Hansen et al., 2006] by

$$\mathbf{F}_{LM} = \mathbf{F}_M \otimes \mathbf{F}_L.$$

In practice, the Kronecker product does not have to be evaluated. To compute the DFT of an image, the one dimensional FFT algorithm is applied first to the image's columns and then to the rows of the result or vice versa.

In conclusion, the computational cost to compute a two-dimensional Fourier transform using the FFT algorithm on images of size of a power of two is $\mathcal{O}(N \log_2(N))$, where N is the number of pixels in the image.

3.4.2 Modified Overlap-Add to Reduce the Problem Size

The previous section has shown that the computational cost of the convolution can be lowered dramatically using the Fast Fourier Transform. In this section we show how we can take advantage of the structure of the point spread functions and the masked vectors $\mathbf{M}_i\mathbf{x}$. The values of the discretized PSFs near the boundaries are close to zero. If values below a threshold are neglected, these images can be considered to have limited support. Binary masked images $\mathbf{M}_i\mathbf{x}$ are also zero outside the selected region.

We take advantage of the structure of the PSFs and the masked images by using the overlap-add approach described in [Oppenheim and Schafer, 1975, p. 113] to decompose the convolution in Equation (3.15). Furthermore, if the spatial variance of the PSFs is taken into account, the overlap add method can be slightly modified to use different convolution kernels.

Given an array $\mathbf{p} \in \mathbb{R}^N$ and an interval $S \subset [1, N]$ such that $\mathbf{p}(l) = 0$ for $l \notin S$ and an image vector $\mathbf{x} \in \mathbb{R}^N$, the one dimensional convolution with zero-boundary conditions

$$\mathbf{b} = \left(\sum_{j \in S} \mathbf{p}(j)\mathbf{x}(l-j) \right)_{l=1,..,N}$$

can be decomposed with help of a partitioning of the interval $[1, ..., N]$ into smaller intervals $\mathcal{M}_i \subset [1, N]$ with $\cup \mathcal{M}_i = [1, N]$ and $\mathcal{M}_i \cap \mathcal{M}_j = \varnothing$ for $i \neq j$. Given such a partitioning, the image vector $\mathbf{x}$ can be decomposed into vectors $\mathbf{x}_i \in \mathbb{R}^N$ such that

$$\mathbf{x}_i(l) = \begin{cases} \mathbf{x}(l) & \text{if } l \in \mathcal{M}_i \\ 0 & \text{otherwise} \end{cases}$$

and the convolution can be written as a sum of smaller convolutions

$$\mathbf{b} = \sum_{i=1}^{k} \left(\sum_{j \in S} \mathbf{p}(j)\ \mathbf{x}_i(l-j) \right)_{l=1,..,N} . \tag{3.19}$$

The inner brace in Equation (3.19) can be evaluated in a few operations because only a few summands are non-zero due to the limited support of $\mathbf{x}_i(l-j)$.

The original overlap-add method takes advantage of the limited region of support of the PSF by splitting up the computation into several smaller problems, each computing the convolution of a partition of the image with the same PSF and adding up the individual results. In the spatial variant case with masked images $\mathbf{M}_i\mathbf{x}$ the non-zero region of these vectors is relatively small. Furthermore, each of these masked images is convoluted with a different PSF.

The modification of the overlap-add method for spatial variance can be understood in two ways. First, only regarding each inner summand in Equation (3.19) separately, the image's partitioning can be chosen according to the masking matrices $\mathbf{M}_i$ such that only one of the partitioned vectors $\mathbf{x}_i$ is non-zero and the outer sum has to be evaluated only once. Alternatively, now regarding the entire convolution, Equation (3.15) could also be interpreted as a modified overlap-add method, where the point spread function for each region is different.

3.4.3 Preconditioning of the Iteration Matrix

Before discussing the application of the methods developed in this thesis to simulated x-ray data, we want to focus on the possibility to speed up the computations by modifying the linear system in Equation (3.16).

As discussed in Section 3.1.3, the convergence of the LSQR method can be very fast if the eigenvalues of $\mathbf{A}$ are organized in clusters. One way to accelerate the convergence of the iteration is to modify the system

$$\mathbf{b} = \mathbf{A}\mathbf{x} = \mathbf{W}^{-1}\sum_{i=1}^{k}\mathbf{A}_i\mathbf{M}_i\mathbf{x}$$

such that the clustering of the eigenvalues of $\mathbf{A}$ is increased but the solution stays the same. One way to achieve this is to multiply both sides of the linear system by a matrix $\mathbf{C}^{-1}$ such that $\mathbf{C} \approx \mathbf{A}$ such that the system is easier to solve [Benzi, 2002].

The one PSF that is most similar to every other PSF corresponds to a point source located at the detector center (cf. Figure 2.3, left image). Numerical experiments have shown that this PSF can be used as a basis for a preconditioner as it is approximately symmetric and represents common features from all PSFs. Let $\mathbf{A}_s$ be the circular convolution matrix

encoding this symmetric PSF. As this matrix also has small singular values, noise would be amplified by its inverse if it was applied directly as a preconditioner. Therefore, we chose a preconditioning matrix $\mathbf{C} \approx \mathbf{A}_s = \mathbf{F}^* \mathbf{\Lambda}_s \mathbf{F}$ that is based on $\mathbf{A}_s$ but that is spectrally truncated with

$$\mathbf{C} = \mathbf{F}^* \, \mathbf{\Lambda}_C \, \mathbf{F}, \text{where}$$
$$(\mathbf{\Lambda}_C)_{i,i} = \begin{cases} (\mathbf{\Lambda}_s)_{i,i} & \text{if } (\mathbf{\Lambda}_s)_{i,i} > \tau \\ 1 & \text{otherwise} \end{cases}.$$

This preconditioner can be applied to Equation (3.14) and we obtain a new system of the form

$$\mathbf{C}^{-1}\mathbf{b} = \mathbf{W}^{-1} \sum_{i=1}^{k} \mathbf{F}^* \, \mathbf{\Lambda}_C^{-1} \mathbf{\Lambda}_i \, \mathbf{F} \, \mathbf{M}_i \, \mathbf{x}.$$

Numerical experiments have shown that the reduction in the number of iterations is most noticeable if the preconditioner is used on linear systems that are larger than the ones used in the image reconstruction problem analyzed in this work. For systems corresponding to image sizes of 200×200 pixels only a few number of iterations are needed to solve the unpreconditioned system and the benefit from the preconditioning is limited. Furthermore, the choice of the parameter τ is not obvious as too small values lead to an amplification of noise but larger values limit the improvements in convergence speed. For these reasons, preconditioning is not further analyzed in this thesis but future work could benefit from further analysis.

4 Application of the Forward Model to Artificial X-Ray Imaging Data

This chapter deals with the application of the forward model to create a blurred image $\mathbf{b}$ from a hypothetical true image $\mathbf{x}$. Therefore, the application of the point spread function interpolation and the model for the image blurring process in a simulated x-ray detector are described. In these simulations, different scintillator thicknesses and energy parameters are used. The results of the backward problem consisting of the reconstruction of an approximated image $\hat{\mathbf{x}}$ from an acquired image $\mathbf{b}$ are are presented in Chapter 5.

The following four steps are executed in the forward model to simulate an acquired image $\mathbf{b}_{highres}$ originating from a known high resolution true image $\mathbf{x}_{highres}$.

1. Generate 6 PSF samples with MANTIS according to scintillator thickness and energy parameter. Choose the position of high resolution true test pattern stored in an array $\mathbf{x}_{highres}$ on the detector.

2. Create 128×128 point spread functions $\mathbf{P}_i, i = 1, ..., 128^2$ from 6 samples by interpolation and rotation.

3. Create masks $\mathbf{M}_i$ and select corresponding PSFs.

4. Blur $\mathbf{x}_{highres} \curvearrowright \mathbf{b}_{highres} = \mathbf{A}\mathbf{x}_{highres}$.

The details for each step are given in the following sections.

Point Spread Functions Describing the Image Degradation

The basis for our evaluations are sets of six PSF images, each set corresponding to a simulated x-ray imaging system with the parameters shown in Table 4.1 that were computed with MANTIS in the scope of the joint work with James Nagy and Ioannis Sechopoulos.

Table 4.1: Parameters used to simulate the x-ray imaging device. Each pair of scintillator thickness and x-ray energy parameter is used to create 6 PSFs with MANTIS.

Parameter	Value
detector size	$41cm \times 41cm$
scintillator thickness (d_1, d_2) in mm	$(0.1, 0.5), (0.1, 1.0), (0.1, 1.5), (0.1, 2.0)$ $(0.05, 0.5), (0.15, 1.5), (0.2, 2.0)$
x-ray energy	65.0 keV, 57.5 keV
distance of point source from center	0cm, 5cm, 10cm, 15cm, 22cm ,29cm
resolution of point spread function	20 µm/pixel

The point sources corresponding to these samples are located between the center of the detector surface and its lower right corner. The PSF consists basically of two Gaussians, one broader in the center and the other very narrow located towards the lower right corner of the image. See Figure 4.1 for a visualization of these images and their respective point source positions.

The interpolation framework introduced in Section 3.3 will be used to calculate the transitions between the PSF image samples. To determine how many PSFs are necessary to simulate the blur caused by the x-ray imaging system, we make the following assumptions. Due to the construction of the detector as shown in Figure 2.2, the shape of the PSF is rotated if the position of the point source changes on a circle around the center. If the distance of the point source to the center of the detector increases, the narrower Gaussian is moved in the same direction as the point source and the broader of the two Gaussians gets stretched towards the narrower one. Numerical experiments have shown that the PSF does not change significantly if the point source moves less than $2mm$ in radial direction or less than 3° in angular direction, which corresponds to using 128×128 different PSFs.

Circular Masking to Discretize Spatial Variance

For each of the PSF images created by the interpolation framework, the corresponding region in the image is selected by a diagonal masking matrix. The masking matrices are defined according to the assumptions of local spatial invariance. As the two parameters that influence the shape of the PSF are distance of the point source from the detector center and the angle on the circle around the center, the difference of the PSFs can be described best in a polar coordinate system. On a detector of a size of $41cm \times 41cm$, we

Listing 4.1: Matrix multiply with two-dimensional Fourier transforms in MATLAB pseudo code.

```
for i=1:k
  c=findCenter(P(:,:,i))
  B = B + ifft2(fft2(circshift(P(:,:,i),1-c)) .* fft2(M(:,:,i).*X)))
end
B=B./W + simulateNoise()
```

produce 128×128 regions that are shown in Figure 4.2. However, the blurring process has been implemented in a Cartesian and not in a polar grid to prevent discretization errors that would occur especially in the detector center.

Implementation of Matrix Multiplications

With the PSF images and the masking matrices, all the information needed to simulate the image blur caused by the x-ray detector is given. Because of the previously introduced circular masks, the modified overlap-add method introduced in Section 3.4.2 has to be extended slightly to cope with non-rectangular regions.

To implement the overlap-add method on non-rectangular regions, these regions are embedded in the smallest possible rectangle. To find this rectangle, the masked region is projected orthogonally onto each axis. The minimal rectangle resulting from the projected coordinates is extended at each edge by the size of the minimal rectangle containing the point spread function. Every pixel outside of the resulting region can be set to zero, reducing the computation time spent on the Fourier transform dramatically.

To reduce the computational cost, we do not build up the matrices $\mathbf{A}_i$, $\mathbf{M}_i$ or $\mathbf{W}$. The diagonal masking and weighting matrices $\mathbf{M}_i$ and $\mathbf{W}$ can be applied by element-wise multiplication of the diagonal to the image. In the pseudo code below, each mask is stored in a slice `M(:,:,i)`, $i = 1, ..., k$ of a three dimensional array `M` such that the masking can be achieved by element wise multiplication with the image stored in an two dimensional array `X`. Using an FFT algorithm on the masked image and the PSFs $\mathbf{P}_i$ stored in slices `P(:,:,i)` of a three dimensional array `P`, Equation (3.16) can be implemented as shown in Listing 4.1.

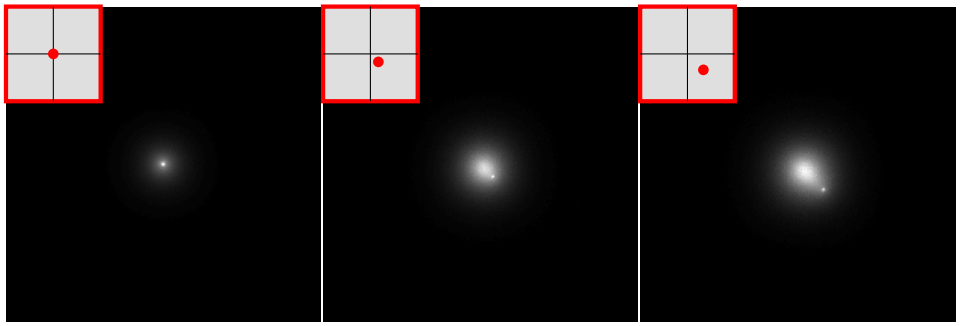

(a) 0 cm (b) 5 cm (c) 10 cm

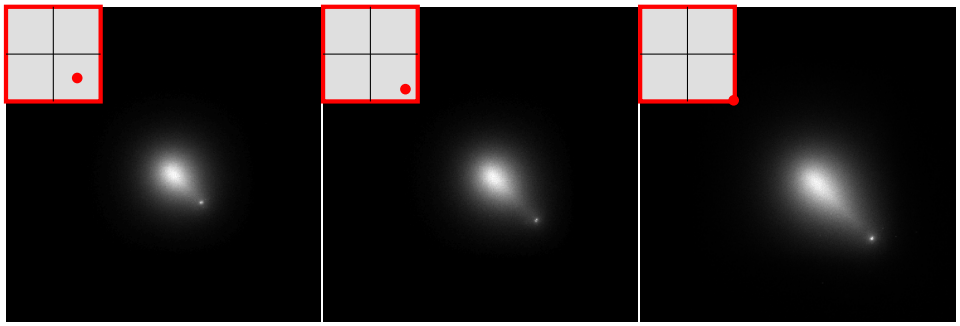

(d) 15 cm (e) 22 cm (f) 29 cm

Figure 4.1: Initial Point spread functions generated using MANTIS with given distances of the point source (red dot) to the detector center.

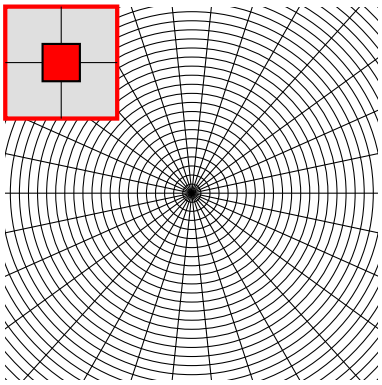

Figure 4.2: Plot of regions in which spatial invariance is assumed. Each cell corresponds to a region that is selected by a diagonal masking matrix $\mathbf{M}_i$. The plot shows the magnified center region of the detector marked by the red box.

Resolution Levels to Model Discretized Image Acquisition

To fully reproduce the behavior of the x-ray detector, the limited resolution of the photodetector and the perturbations caused by noise have to be taken into account.

In order to precisely simulate this part of the physics of the x-ray detector, both PSFs and blurred images are created in a resolution of 20 μm/pixel which is approximately ten times higher than in realistic imaging situations. To realistically simulate an acquired image using different scintillator thicknesses, the ideal images are blurred with the interpolated PSFs at the high resolution conditions (20 μm/pixel) and then binned to the pixels size of the detector being studied (200 μm/pixel). Next, the appropriate values of noise are added based on Saunders' algorithm [Saunders Jr and Samei, 2003]. The appropriate simulation of noise occurring in an x-ray detector involves detailed knowledge of the detector physics and is not in the scope of this thesis but part of the joint work with James Nagy and Ioannis Sechopoulos.

5 Evaluation of Calculated PSFs and Restored Images

In this chapter, the calculated PSFs and the image restoration developed in this work is evaluated. In Section 5.1 the interpolation scheme is tested by comparing the interpolated PSF images with simulations generated additionally with MANTIS. In the second part, in Section 5.2, deblurred images resulting from the image reconstruction method are evaluated in terms of relative error and different image features.

5.1 Interpolation of Spatially Variant Point Spread Functions

To test the PSF interpolation method, we compare a PSF that has been predicted by our algorithm with the corresponding PSF created by Monte Carlo simulations. The difference image in Figure 5.1 shows that the approximate form of the PSF is very similar to the simulated PSF created with MANTIS. Only the position of the narrow peak tends to be shifted slightly if the point source is more distant from the detector center. The largest difference between the two PSF images is below 20% of the maximal pixel value in the simulated PSF. As shown in Figure 5.2, images blurred by each of these PSFs do not show any visual differences.

5.2 Reconstruction of Simulated X-Ray Images

In the rest of this chapter, results for a simulated x-ray reconstruction are presented. In the first part, the improvement of the relative error of the reconstructed image is analyzed for different scintillator thicknesses and detector parameters. In the second part we analyze the contrast transfer function of the reconstructed image and also observe an improvement in the image's quality.

(a) interpolated PSF ($\mathbf{P}_{intp}$) (b) simulated PSF ($\mathbf{P}_{mc}$) (c) difference image ($\frac{|\mathbf{P}_{intp}-\mathbf{P}_{mc}|}{\max(\mathbf{P}_{mc})}$)

(d) interpolated PSF ($\mathbf{P}_{intp}$) (e) simulated PSF ($\mathbf{P}_{mc}$) (f) difference image ($\frac{|\mathbf{P}_{intp}-\mathbf{P}_{mc}|}{\max(\mathbf{P}_{mc})}$)

Figure 5.1: Comparison of simulated and interpolated PSFs. Distance from detector center: (a - c) 5.3 cm (d -f) 12.4 cm.

To test the reconstruction method, we use an artificial image consisting of line patterns of different frequencies. This test pattern has 16 equally sized blocks, each of a different spatial frequency, ranging from 0.25 to 4.5 line pairs per millimeter. The contrast of this image is chosen to be 60%. See Figure 5.3a for details.

We first generate an approximation of the acquired image by blurring the test image with 128×128 PSFs (in radial and angular direction) at a resolution of 20 µm/pixel (2100×2100 pixels), which is ten times higher than the resolution that is available to currently used general radiography x-ray detectors. In a clinical application, it is impossible to measure all the information involved in the image acquisition which means that not all of it is available for the reconstruction. We take this loss of information into account and show that the method developed in this work can still reconstruct a good approximation to the underlying true image with a lower number of point spread functions and at a lower

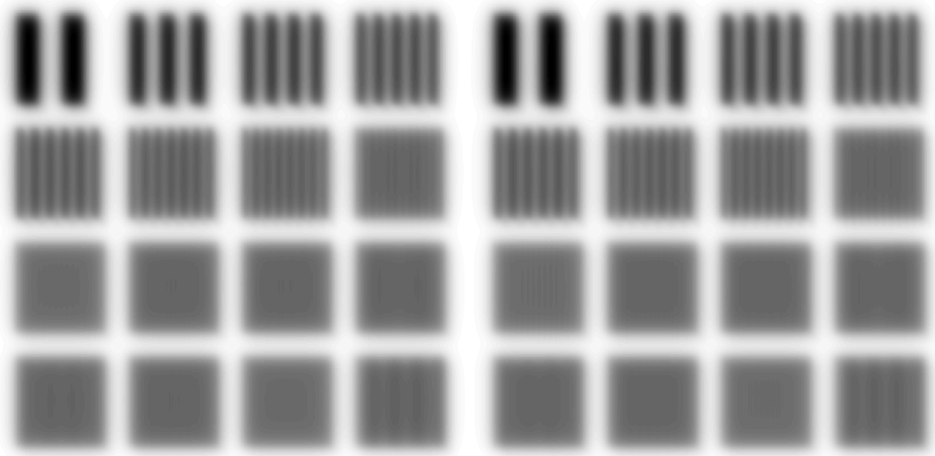

(a) blurred with interpolated PSF ($\mathbf{B}_{intp}$) (b) blurred with simulated PSF ($\mathbf{B}_{mc}$)

Figure 5.2: Test pattern blurred spatially invariant with estimated and simulated PSF at distance from detector center of 12.4 cm. The images show no visual difference, the relative error is below 1%.

image resolution.

To lower the resolution we use binning on both the interpolated PSF images and the acquired image, which is consistent to the physical image detection process in which all light photons leaving the scintillator are summed up in pixels. We use quadratic bins with sizes of 10×10 pixels to lower the image size to 210×210 pixels. Colored noise is added to the low resolution acquired image to account for inaccuracies introduced by the digital photodetector as previously described.

The algorithm presented in Chapter 4 to compute the forward model can be extended with the reconstruction in steps 5 and 6. The complete algorithm to simulate image degradation and perform a reconstruction is summarized as follows.

1. Generate 6 PSF samples with MANTIS according to scintillator thickness and energy parameter. Choose the position of high resolution true test pattern stored in an array $\mathbf{x}_{highres}$ on the detector.

2. Create 128×128 point spread functions $\mathbf{P}_i, i = 1, ..., 128^2$ from 6 samples by interpolation and rotation.

3. Create masks $\mathbf{M}_i$ and select corresponding PSFs.

4. Blur $\mathbf{x}_{highres} \curvearrowright \mathbf{b}_{highres} = \mathbf{A}\mathbf{x}_{highres}$.

5. Downsample $\mathbf{b}_{highres}$ and add realistic noise $\mathbf{b}_{highres} \overset{+\mathbf{n}}{\curvearrowright} \mathbf{b}$.

6. Deblur $\mathbf{b} \curvearrowright \hat{\mathbf{x}}$ with the original number and also with a lower number of PSFs.

The resulting reconstructed image is compared to a downsampled true image $\mathbf{x}_{true}$ to evaluate the quality of the reconstruction.

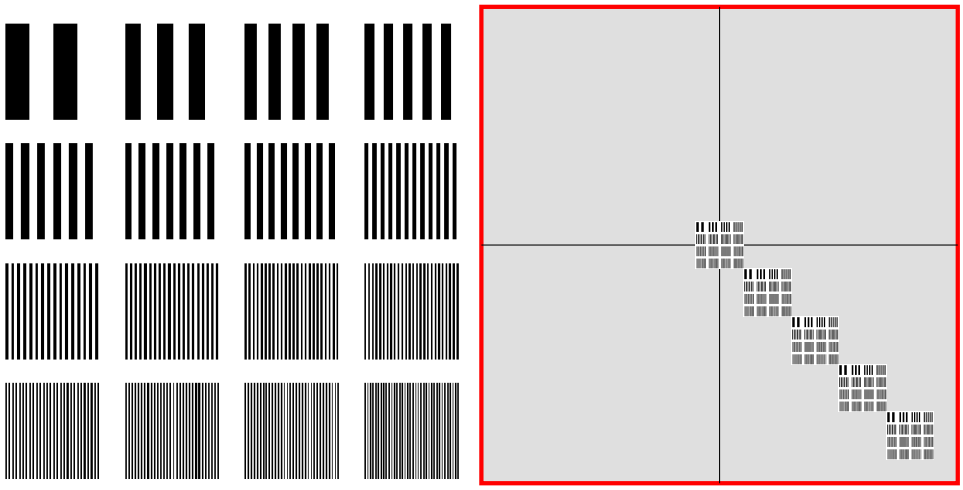

(a) (b)

Figure 5.3: Test pattern consisting of lines of different frequencies (a), placed at different distances from the detector center (b).

5.2.1 Analysis of the Relative Error

To evaluate the success of our model on different parts of the image, we blur and reconstruct the test pattern at different positions on the detector as shown in Figure 5.3b. At each step of an LSQR iteration we calculate the relative error between the current iterate $\mathbf{x}_{step}$ and the known true image $\mathbf{x}_{true}$ which is obtained by downsampling $\mathbf{x}_{highres}$,

$$e_2 = \frac{\|\mathbf{x}_{step} - \mathbf{x}_{true}\|_2}{\|\mathbf{x}_{true}\|_2}.$$

We analyze the relative error in the reconstructed image at different positions on the detector and for different scintillator thicknesses.

The error curves in Figure 5.4 show an increasing separation if the test pattern is moved towards the edge of the detector ((a) to (d)). This is mainly caused by the stronger deformation of the image in these regions due to the broader PSFs (cf. Figure 4.1) and the increased difference between PSFs of neighboring grid cells. At a larger distance from the detector center, the point spread functions have a larger effect and a coarser discretization of the spatial variance increases the approximation error. For further analysis, we focus on a distance of 11.88 cm from the detector.

A similar observation can be made in Figure 5.5. The scintillator thickness is increasing from (a) to (c) and from (d) to (f). As the scintillator size increases, the PSFs broaden and the spatial variance decreases. This correlation seems surprising at first, but is explained by the two different Gaussian shapes in the PSFs. In thinner scintillator crystals, the expression of the main Gaussian is weaker and the narrow Gaussian has a larger influence on the quality of the blur. This increases the spatial variance in the blur, causing a higher approximation error in coarse approximations. We choose the scintillator used in (e) in Figure 5.5 as an intermediate example for further analysis.

Furthermore, we choose 16×16 (red line, dashed $--$) as the number of PSF to use for the reconstruction. This choice offers good error reduction while still using only $\frac{1}{64}$ of the PSFs used in the forward model, hence respecting the fact that not all information will be available in the reconstruction. In particular we observe, that the error is significantly lower compared to the case where only one PSF is used and spatially invariance is assumed.

We also calculated a total variation based error measure

$$e_{TV} = \frac{\mathrm{TV}(\mathbf{x}_{step} - \mathbf{x}_{true})}{\mathrm{TV}(\mathbf{x}_{true})}, \text{ where}$$
$$\mathrm{TV}(\mathbf{x}) = \|\frac{\partial \mathbf{x}}{\partial x}\|_1 + \|\frac{\partial \mathbf{x}}{\partial y}\|_1.$$

Using central differences, $\frac{\partial \mathbf{x}}{\partial x}$ and $\frac{\partial \mathbf{x}}{\partial y}$ approximate the derivative along the first and second dimension of the two dimensional array represented by the vector $\mathbf{x}$. In contrast to the two norm e_2 of the relative error calculated above, total variation based error measures such as e_{TV} better distinguish oscillating error patterns [Aubert and Aujol, 2005] which are undesirable in some situations. This error measure shows similar results to the plots of e_2 shown in Figure 5.6. The minimum of the total variation based error curves is obtained at an earlier iteration which is due to larger influence of noise to e_{TV} than to e_2.

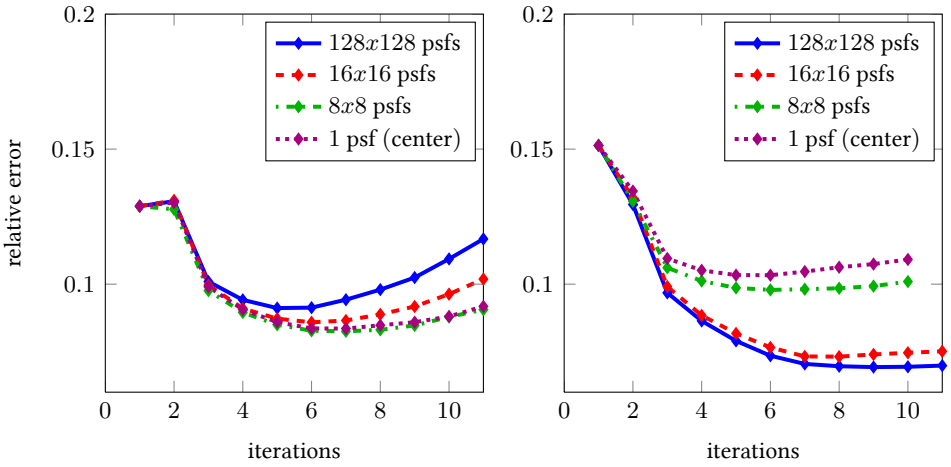

(a) 0 cm (b) 5.94 cm

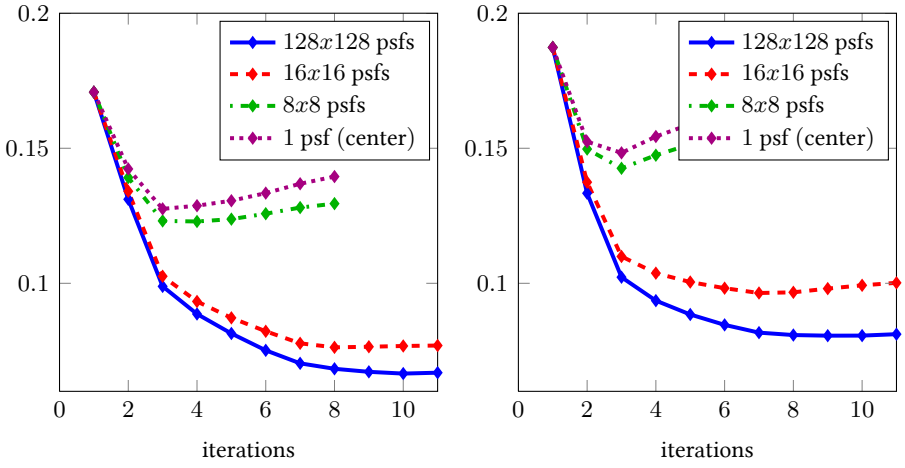

(c) 11.88 cm (d) 17.82 cm

Figure 5.4: Relative error per LSQR iteration for different numbers of PSFs at **different detector locations**: (solid line, blue) 128×128 PSFs, (dashed line $--$, red) 16×16 PSFs, (point-dashed $\cdot-$, green) 8×8 PSFs , (dotted $\cdots$, purple) 1 PSF at detector center. Distance of test pattern from center growing from (a)-(d). PSFs simulated with a scintillator thickness of $d_1 = 0.15$mm and $d_2 = 1.5$mm.

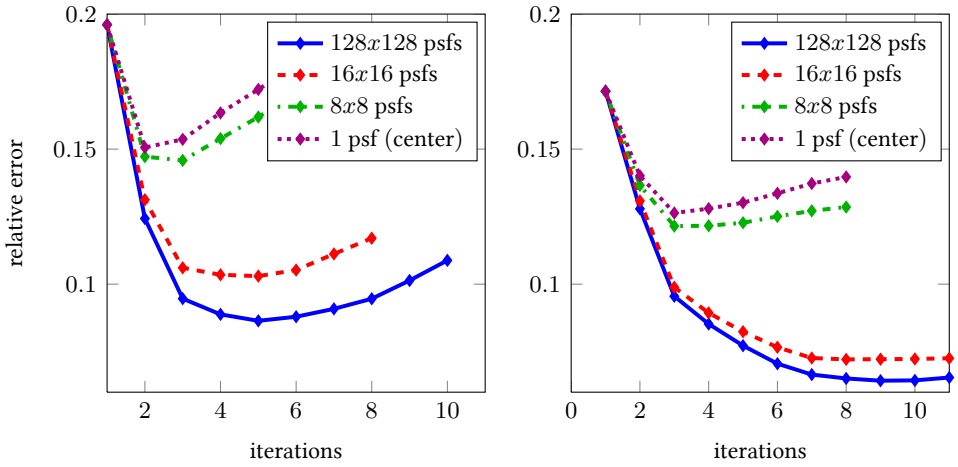

(a) $d_1 = 0.1$mm, $d_2 = 1.0$mm

(b) $d_1 = 0.1$mm, $d_2 = 1.5$mm

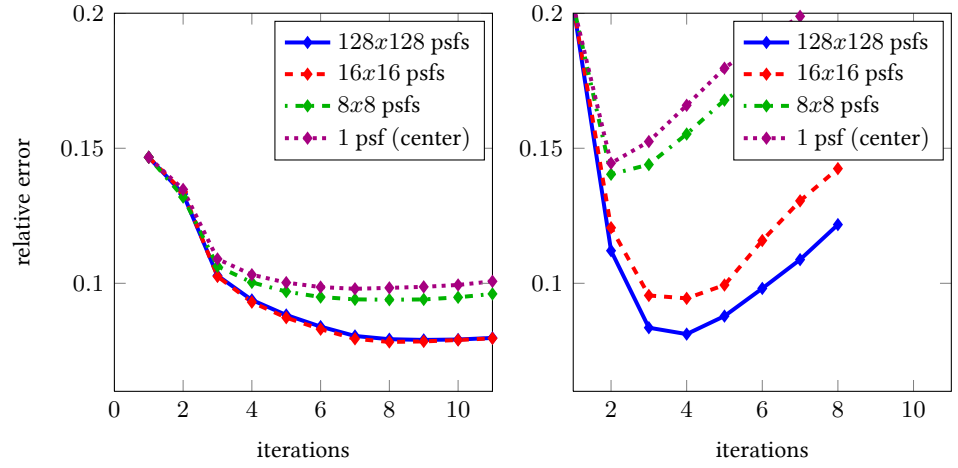

(c) $d_1 = 0.1$mm, $d_2 = 2.0$mm,

(d) $d_1 = 0.05$mm, $d_2 = 0.5$mm

Figure 5.5: Relative error per LSQR iteration for different numbers of PSFs for **different scintillator parameters**: (solid line, blue) 128×128 PSFs, (dashed line $--$, red) 16×16 PSFs, (point-dashed $\cdot-$, green) 8×8 PSFs , (dotted $\cdots$, purple) 1 PSF at detector center. Scintillator parameters growing from (a)-(c) and (d)-(f). Test image at distance of 11.88 cm from detector center. This figure is continued on the following page.

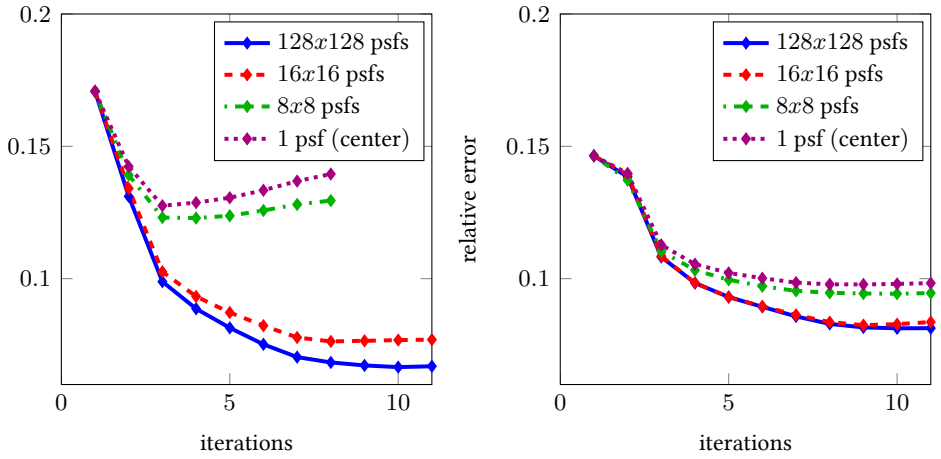

(e) $d_1 = 0.15$mm, $d_2 = 1.5$mm (f) $d_1 = 0.2$mm, $d_2 = 2.0$mm

Figure 5.5: Continued from previous page: Relative error per LSQR iteration for different numbers of PSFs for **different scintillator parameters**: (solid line, blue) 128×128 PSFs, (dashed line $--$, red) 16×16 PSFs, (point-dashed $\cdot-$, green) 8×8 PSFs , (dotted $\cdots$, purple) 1 PSF at detector center. Scintillator parameters Scintillator parameters growing from (a)-(c) and (d)-(f). Test image at distance of 11.88 cm from detector center.

The iteration number can be interpreted as the regularization parameter such that earlier iterations are likely to contain less noise.

5.2.2 Improvements in Image Contrast

The reconstructed image also allows better isolation of the individual lines, as it can be seen in a profile plot in Figure 5.7. The profile plot shows a columnwise average of 3 rows from the first four patterns. To be able to measure the improvement reliably, we calculate contrast transfer functions of all line patterns. We define the contrast transfer function $c(\mathbf{x}, \mathbf{x}_{true}, \mathcal{R})$ of an image $\mathbf{x}$ limited to the rectangular region defined by the index set $\mathcal{R} \subset \{1, ..., N\}$ as

$$
\begin{aligned}
c(\mathbf{x}, \mathbf{x}_{true}, \mathcal{R}) &= \frac{\text{avgmax}(\mathbf{x}, \mathcal{R}) - \text{avgmin}(\mathbf{x}, \mathcal{R})}{\text{avgmax}(\mathbf{x}_{true}, \mathcal{R}) - \text{avgmin}(\mathbf{x}_{true}, \mathcal{R})}, \text{ where} \\
\text{avgmax}(\mathbf{x}, \mathcal{R}) &= \text{mean}(\{\mathbf{x}(n) \,|\, n \in \mathcal{R},\, \mathbf{x}(n) > \text{mean}(\mathbf{x})\}) \text{ and} \\
\text{avgmin}(\mathbf{x}, \mathcal{R}) &= \text{mean}(\{\mathbf{x}(n) \,|\, n \in \mathcal{R},\, \mathbf{x}(n) < \text{mean}(\mathbf{x})\}).
\end{aligned}
$$

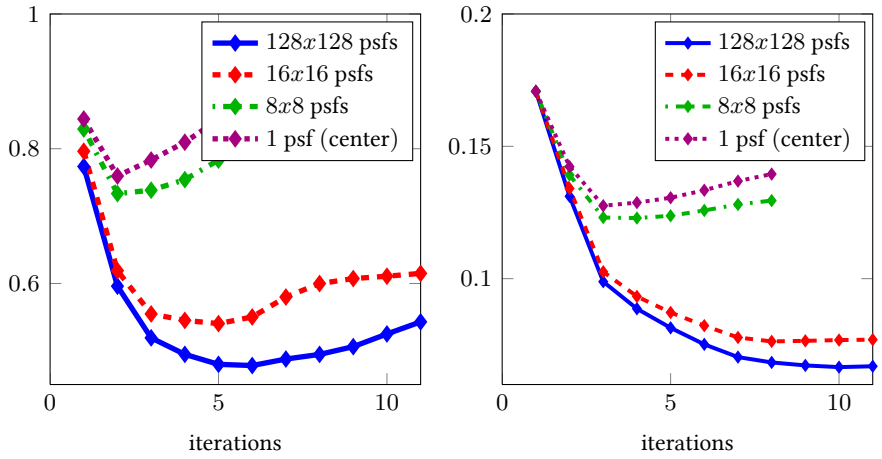

(a) total variation based error measure

(b) relative error

Figure 5.6: Comparison of a **total variation based error measure with the relative error** for the same reconstruction parameters for different scintillator parameters: (solid line, blue) 128×128 PSFs, (dashed line $--$, red) 16×16 PSFs, (point-dashed $\cdot-$, green) 8×8 PSFs , (dotted $\cdots$, purple) 1 PSF at detector center. of 17.82 cm from detector center.

The contrast transfer functions in Figure 5.8 show that the reconstructed image enhances the contrast in line patterns up to a frequency of about 2 line pairs per millimeter. A comparison of the reconstructed images from the 2mm-thick scintillator with the acquired images from the thinner 0.5mm-scintillator, shows that the contrast transfer function is still improved for low line pair frequencies. This remarkable result shows that our reconstruction algorithm can indeed be used to partly compensate undesired effects of thicker scintillator crystals. Contrast improvement is unlikely for line pair frequencies beyond the Nyquist frequency of $\frac{1}{2 \cdot 20 \mu m} = 2.5\ \text{mm}^{-1}$. Finer patterns are neither distinguishable in the acquired nor in the reconstructed image. As a conclusion, Figure 5.9 shows the true image next to the acquired and reconstructed images. The magnification shows the visual improvement due to the reconstruction.

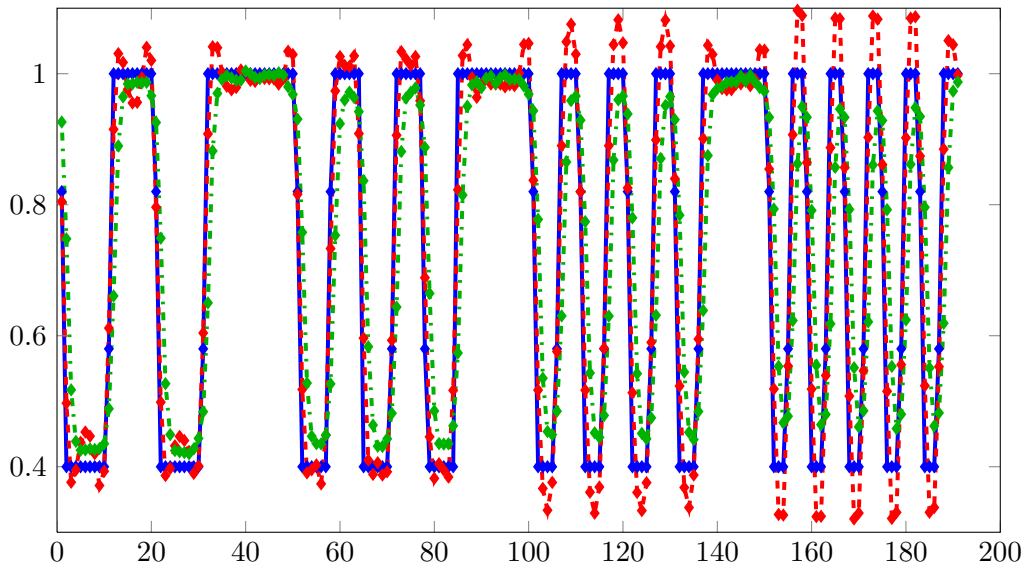

Figure 5.7: Profile through the first four line patterns of the reconstructed image after 3 iterations. (solid line, blue) true image, (dashed line $--$, red) reconstructed image, (point-dashed $\cdot-$, green) acquired image before reconstruction. Scintillator: $d_1 = 0.15$mm, $d_2 = 1.5$mm. Distance from center of detector: 11.88 cm. 16×16 PSFs used for reconstruction.

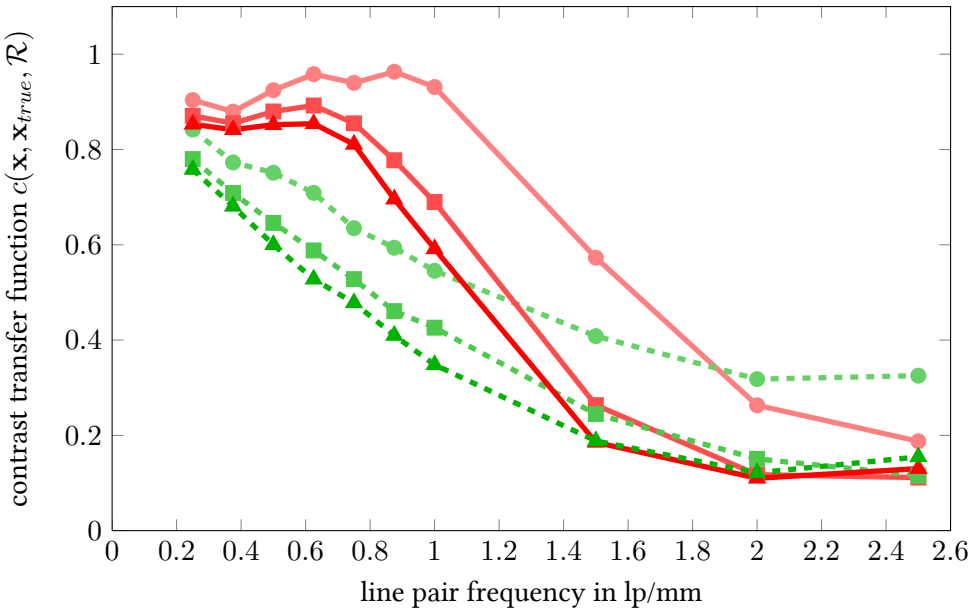

Figure 5.8: Contrast transfer functions for patterns up to the Nyquist frequency of 2.5lp/mm of the acquired and reconstructed image for 3 scintillator thicknesses. (solid line, red) reconstructed image, (dashed −−, green) acquired image before reconstruction. Scintillator thickness from top to bottom in each color: (circular markers) $d_2 = 0.5$mm, (square markers) $d_2 = 1.5$mm, (trianglular markers) $d_2 = 2.0$mm. Distance from center of detector: 11.88 cm. 16×16 PSFs used for reconstruction.

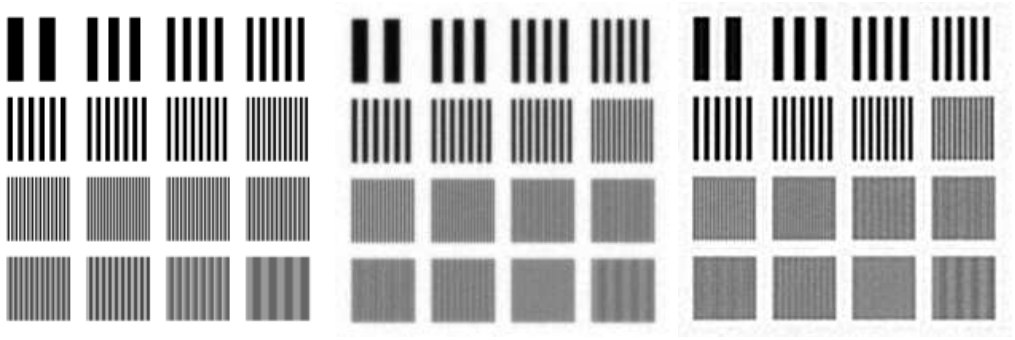

(a) Ground truth. (b) Acquired image. (c) Reconstructed image.

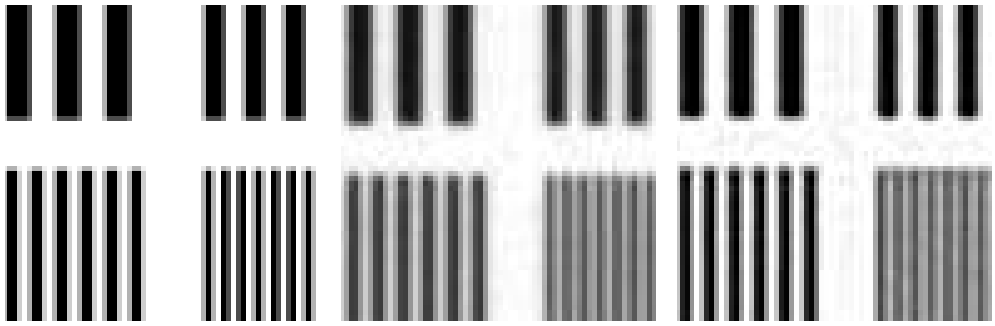

(d) Ground truth (magnified). (e) Acquired image (magn.). (f) Reconstructed img. (magn.).

Figure 5.9: Images involved in reconstruction: (a) Ground truth image $\mathbf{x}$, (b) acquired, blurred image $\mathbf{b}$, (c) reconstructed image $\hat{\mathbf{x}}$ and magnifications (d)-(f). Scintillator parameters: $d_1 = 0.15$mm, $d_2 = 1.5$mm. 16×16 PSFs. Test image at distance of 11.88 cm from detector center. The tenth line pattern in each of (a), (b), and (c) corresponds to 2.5 line pair per mm spatial frequency, which is the Nyquist frequency of the simulated photodetector.

6 Conclusion and Outlook

Crystal scintillators are widely used in digital radiography [Moore, 2001; Samei and Flynn, 2003] and are not only important in clinical but also in industrial applications [Franco et al., 2011; Kim et al., 2009]. In this work, we have modeled the blur introduced in the acquired images by these detectors as an image restoration problem based on spatially variant deconvolution. Using this model, we have developed a method to reconstruct image degradation caused by thick scintillators. The results suggest that the construction of x-ray detectors with higher quantum efficiency is possible due to the recovery of image quality by the presented algorithm. This could be beneficial in medical diagnostics as the radiation dose to patients examined with these detectors is significantly lower.

For given x-ray detector parameters, a small number of PSF images can be simulated by Monte Carlo methods. With the interpolation framework developed in this work, the remaining information required to perform an image reconstruction can be estimated in form of additional PSFs. The presented spatially variant deconvolution approach has proved to be superior to a simple spatially invariant reconstruction and to increase image quality and contrast in the reconstructed image.

Most importantly, the compensation is superior to the quality of images that were recorded conventionally with thinner scintillators. This result suggests that our method can be used to increase the quantum efficiency of x-ray detectors and to lower the radiation dose a patient has to be exposed to.

In future work, the approximation of the spatial variance of $p(\mathbf{s}, \mathbf{t})$ by a piecewise constant model could be improved. This could be extended to linear or higher order approximations. Furthermore, all computations have been implemented with Fourier methods which enforces circular boundary conditions on the images. Different boundary conditions can be used by extending the image beyond the boundaries and calculating the convolution with the resulting larger images. If different boundary conditions are used, other implementations could be studied that might not require an extension of the image.

In the evaluations of the reconstruction process the underlying ground truth image is

always known such that the error of the approximation can be calculated exactly and the optimal number of iterations of the LSQR algorithm can be determined by an error measure. However, if real life test data is used in future work, the true image will not be available and reliable stopping criteria will be needed. Possible methods such as the L-curve [Hanke and Nagy, 1996] could be investigated. The same applies to error bounds of the approximated solution that have not been addressed.

The possibilities of preconditioning the iteration matrix have only been covered very briefly and further development such as in [Nagy et al., 1998] could improve the convergence rate while maintaining the regularizing properties of the LSQR method.

The presented results are based upon simulations and artificial data. We are looking forward to test the presented methods on real-life data. Such tests are one of the next steps to evaluate the performance of our method on the way towards its application in a clinical setting. The current results have been presented to industrial partners and were evaluated positively.

Bibliography

A. Assmus. Early history of x rays. *Beam Line*, 25(2), 1995.

G. Aubert and J.F. Aujol. Modeling very oscillating signals. application to image processing. *Applied Mathematics & Optimization*, 51(2):163--182, 2005.

A. Badano. Image quality degradation by light scattering processes in high performance display devices for medical imaging. *Medical Physics*, 26:1020, 1999.

A. Badano and J. Kanicki. Monte carlo analysis of the spectral photon emission and extraction efficiency of organic light-emitting devices. *Journal of Applied Physics*, 90:1827, 2001.

A. Badano and J. Sempau. MANTIS: Combined x-ray, electron and optical Monte Carlo simulations of indirect radiation imaging systems. *Physics in Medicine and Biology*, 51: 1545, 2006.

P. Baldelli, J. McCullagh, N. Phelan, and F. Flanagan. Results of comprehensive dose survey for mammography. *Digital Mammography*, pages 70--77, 2010.

M. Benzi. Preconditioning techniques for large linear systems: a survey. *Journal of Computational Physics*, 182(2):418--477, 2002.

J. Bernier, E.J. Hall, and A. Giaccia. Radiation oncology: a century of achievements. *Nature Reviews Cancer*, 4(9):737--747, 2004.

K. Binder and D.W. Heermann. *Monte Carlo simulation in statistical physics: an introduction*. Springer, 2010.

R. Bracewell. The fourier transform and its applications. 1978.

E.O. Brigham and RE Morrow. The fast Fourier transform. *Spectrum, IEEE*, 4(12):63--70, 1967. ISSN 0018-9235.

H.G. Chotas, J.T. Dobbins, and C.E. Ravin. Principles of digital radiography with large-area, electronically readable detectors: a review of the basics. *Radiology*, 210(3):595, 1999.

J. Chung and J.G. Nagy. An efficient iterative approach for large-scale separable nonlinear inverse problems. *SIAM Journal on Scientific Computing*, 31:4654, 2010.

P.J. Davis. *Circulant matrices*. Chelsea Pub Co, 1994.

A.B. de González and S. Darby. Risk of cancer from diagnostic x-rays: estimates for the uk and 14 other countries. *The Lancet*, 363(9406):345--351, 2004. 0.6 (uk) - 3% (in japan) of death rate at 75 years are attributed to diagnostic x-ray.

A. Doicu, T. Trautmann, and F. Schreier. *Numerical Regularization for Atmospheric Inverse Problems*. Springer Verlag, 2010.

L. Franco, F. Gomez, A. Iglesias, and F. Vidal. Industrial radiography and tomography based on scanning linear scintillator array. *International Journal of Materials and Product Technology*, 41(1):61--74, 2011.

Matteo Frigo and Steven G. Johnson. The design and implementation of FFTW3. *Proceedings of the IEEE*, 93(2):216--231, 2005. Special issue on ``Program Generation, Optimization, and Platform Adaptation''.

G. Golub and W. Kahan. Calculating the singular values and pseudo-inverse of a matrix. *Journal of the Society for Industrial and Applied Mathematics: Series B, Numerical Analysis*, pages 205--224, 1965.

G.H. Golub, F.T. Luk, and M.L. Overton. A block lanczos method for computing the singular values and corresponding singular vectors of a matrix. *ACM Transactions on Mathematical Software (TOMS)*, 7(2):149--169, 1981.

M. Hanke. On lanczos based methods for the regularization of discrete ill-posed problems. *BIT Numerical Mathematics*, 41(5):1008--1018, 2001.

M. Hanke and J.G. Nagy. Restoration of atmospherically blurred images by symmetric indefinite conjugate gradient techniques. *Inverse problems*, 12:157, 1996.

M. Hanke, J. Nagy, and R. Plemmons. Preconditioned iterative regularization for ill-posed problems. *L. Reichel, A. Ruttan and RS Varga, de Gruyter, Berlin*, pages 141--163, 1993.

P.C. Hansen. Truncated singular value decomposition solutions to discrete ill-posed problems with ill-determined numerical rank. *SIAM Journal on Scientific and Statistical Computing*, 11:503, 1990.

P.C. Hansen. Numerical tools for analysis and solution of fredholm integral equations of the first kind. *Inverse problems*, 8:849, 1992.

P.C. Hansen. *Rank-deficient and discrete ill-posed problems: numerical aspects of linear inversion.* Number 4. Society for Industrial Mathematics, 1998.

P.C. Hansen, J.G. Nagy, and D.P. O'Leary. *Deblurring images: matrices, spectra, and filtering.* Fundamentals of algorithms. SIAM, Society for Industrial and Applied Mathematics, 2006. ISBN 9780898716184.

M.R. Hestenes and E. Stiefel. Methods of conjugate gradients for solving linear systems. *Journal cf Research of the National Bureau of Standards Vol*, 49(6), 1952.

H.S. Kim, J.H. Ha, S.H. Park, S.Y. Cho, and Y.K. Kim. Fabrication and performance characteristics of a csi (tl)/pin diode radiation sensor for industrial applications. *Applied Radiation and Isotopes*, 67(7-8):1463--1465, 2009.

W.R. Leo. *Techniques for nuclear and particle physics experiments: a how-to approach.* Springer, 1994. ISBN 9783540572800.

A. Mertins. *Signaltheorie.* Teubner, 1996.

M. Miller. Cancer imaging: changing focus in the 21st century. *Journal of the National Cancer Institute*, 91(9):759, 1999.

S.K. Moore. Better breast cancer detection. *Spectrum, IEEE*, 38(5):50--54, 2001.

H. Morneburg. *Bildgebende Systeme für die medizinische Diagnostik: Röntgendiagnostik und Angiographie, Computertomographie, Nuklearmedizin, Magnetresonanztomographie, Sonographie, integrierte Informationssysteme.* Publicis MCD Verlag, 2010. ISBN 9783895780028.

VV Nagarkar, TK Gupta, SR Miller, Y. Klugerman, MR Squillante, and G. Entine. Structured csi (tl) scintillators for x-ray imaging applications. *Nuclear Science, IEEE Transactions on*, 45(3):492--496, 1998.

J.G. Nagy, D.P. O'Leary, et al. Restoring images degraded by spatially variant blur. *SIAM Journal on Scientific Computing*, 19(4):1063--1082, 1998. ISSN 1064-8275.

J.G. Nagy, K. Palmer, and L. Perrone. Iterative methods for image deblurring: a matlab object-oriented approach. *Numerical Algorithms*, 36(1):73--93, 2004.

J. Nocedal and S.J. Wright. *Numerical optimization*. Springer verlag, 1999. ISBN 0387987932.

A.V. Oppenheim and R.W. Schafer. Digital signal processing. englewood clis, 1975.

C.C. Paige and M.A. Saunders. Algorithm 583: LSQR: Sparse linear equations and least squares problems. *ACM Transactions on Mathematical Software (TOMS)*, 8(2):195--209, 1982.

J.G. Proakis and D.G. Manolakis. *Digital signal processing: principles, algorithms, and applications*, volume 3. Prentice Hall Upper Saddle River, NJ:, 1996.

Y. Saad. *Iterative methods for sparse linear systems*. PWS Pub. Co., 1996.

F. Salvat, J.M. Fernández-Varea, E. Acosta, and J. Sempau. Penelope. *A code system for Monte Carlo simulation of electron and photon transport, NEA France*, 2003.

E. Samei and M.J. Flynn. An experimental comparison of detector performance for direct and indirect digital radiography systems. *Medical Physics*, 30:608, 2003.

R.S. Saunders Jr and E. Samei. A method for modifying the image quality parameters of digital radiographic images. *Medical physics*, 30:3006, 2003.

A. Smith. Fundamentals of digital mammography: physics, technology and practical considerations. *Radiology management*, 25(5):18, 2003.

VN Strakhov and SV Vorontsov. Digital image deblurring with sor. *Inverse Problems*, 24: 025024, 2008.

M. Strotzer, J.K. Gmeinwieser, M. VÖLK, R. FRÜND, J. Seitz, and S. Feuerbach. Detection of simulated chest lesions with normal and reduced radiation dose: comparison of conventional screen-film radiography and a flat-panel x-ray detector based on amorphous silicon. *Investigative radiology*, 33(2):98, 1998.

A.N. Tikhonov and V.I.A. Arsenin. *Solutions of ill-posed problems*. Winston Washington, DC:, 1977.

A. Webb and G.C. Kagadis. Introduction to biomedical imaging. *Medical Physics*, 30:2267, 2003.